Master of Science

Synthesis of a new cathode material and its characterization using MAS NMR for lithium ion batteries

The Graduate School of the University of Ulsan

Department of Chemistry

Lee, Jiwon

Synthesis of a new cathode material and its characterization using MAS NMR for lithium ion batteries

Supervisor : Professor Youngil Lee

A Dissertation

Submitted to
The Graduate School of the University of Ulsan
In partial Fulfillment of the Requirements
for the Degree of

Master of Science

by

Lee, Jiwon

Department of chemistry
University of Ulsan, Ulsan, Korea

January, 2018

Synthesis of a new cathode material and its characterization using MAS NMR for lithium ion batteries

This certifies that the dissertation of Jiwon Lee is approved.

Committee Chair Dr. Jiwon Ha

Committee Member Dr. Eun-Suok Oh

Committee Member Dr. Youngil Lee

Department of Chemistry

Ulsan, Korea

January, 2018

Abstract

Unlike a primary battery, a secondary battery can be charged and discharged. Thus, it has attracted a great deal of attention in terms of environmental and economic efficiency. Among a secondary battery, Lithium ion battery has lightweight, high power density and high reactivity. Therefore, the aim of this study is to improve the electrochemical performance by studying the cathode of the lithium ion battery. The structural properties of the cathode were characterized by MAS NMR. $Li_3V_2(PO_4)_3$/C is one of the olivine structure material, has excellent structural stability, reversibility and high specific capacity of 197 mAh g^{-1}. However, $Li_3V_2(PO_4)_3$/C has the low electronic conductivity (2×10^{-8} S cm^{-1}) to limit the wide application. To overcome this problem, we have studied the fully substitution using borate. We demonstrate the electrochemical performances of a highly porous $Li_3V_2(BO_3)_3$/C, synthesized via combustion process as a new cathode material. It has a wide range voltage operability ranged from 0.9 to 4.5 V, which deliver exceptionally high discharge capacity of 257 mAh g^{-1} at 0.05 C, 95.6% of its theoretical capacity. The present study will for the novel poly-anion compound of $Li_3M_2(BO_3)_3$/C (M=Al, V, Cr, Fe, Ni and Ga) based on triangular $(BO_3)^{3-}$ unit which is the lightest poly-anion group, could enhance both the theoretical capacity and energy density, also made low lattice volume change during lithiation/delithiation processes. These materials will be promising cathode materials that meet stringent requirements such as high

theoretical capacity, wide voltage operability, low cost, safety and environmental friendliness for the application to electric vehicles (EVs).

내용

List of table

List of figures

NMR [2].

Figure 2.4 Schematic figure of magic-angle sample spinning. (a) A pair of nuclear spins I and S in the solid-state NMR sample tube rotate along the axis tilted magic angle (54.741°) with respect to the external magnetic field. (b) Rotation of the I–S internuclear vector under MAS is expressed by angles a (azimuth angle; rotation of I–S vector around the spinning axis) and b (polar angle; tilt angle between the I–S vector and spinning axis) [3,4].

Figure 2.5 Spin-lattice relaxation (T_1) processes [5].

Figure 2.6 Transverse (T_2 and T_2*) relaxation processes [5].

Figure 2.7 Schematic illustration of 1D NMR pulse sequence. (p1 = pulse width or duration, plw1 = RF field strength, aq = acquisition time and d1 = delay time).

Figure 2.8 The spin-echo pulse sequence [6].

Figure 2.9 ^{6}Li MAS NMR spectra of the spinel $LiMn_2O_4$ based on sintering temperature [7].

Figure 2.10 ^{7}Li MAS NMR spectra of various Li_xCoO_2 ($0.33< x <1$) deintercalated phases recorded with a single-pulse sequence at 13 kHz spinning speed and the spinning sidebands are marked with asterisks (*) [8].

Figure 2.11 (a) ^{7}Li MAS NMR spectra of $LiFePO_4$ (1^{st}) and biphasic $Li_{0.5}FePO_4$ ($0.5LiFePO_4$:$0.5FePO_4$) (2^{nd}). (b) Deconvolution of biphasic $Li_{0.5}FePO_4$ with MAS = 40 kHz and the spinning sidebands are marked with asterisks (*) [9].

Figure 2.12 ^{31}P MAS NMR of $FePO_4$ (top), $LiFePO_4$ (middle) and biphasic $Li_{0.5}FePO_4$ (bottom) all at room temperature. Isotropic shifts for $FePO_4$, $LiFePO_4$ are found at 5800 and 3800 ppm respectively and the spinning sidebands are

Figure 4.8 Cyclic voltammetry during (d) 1st charge –discharge, (d) 2nd charge-discharge and (c) 1st -5st charge - discharge of $Li_3V_2(BO_3)_3$/C.

Figure 4.9 (a) ^{7}Li and (b) ^{51}V MAS NMR spectrum of $Li_3V_2(BO_3)_3$/C at 25kHz. Isotropic peak is marked as arrow and the spinning sidebands are marked with asterisks (*).

1. Introduction of lithium ion battery

Many developments of renewable energy technologies that are contained solar cells, fuel cells, and biofuels and these technologies make more practical alternative energy [10]. The battery is known as energy storage device by converting electric energy with electrochemical reaction. In chemical batteries, a primary cell contained alkaline battery, magnesium battery and mercury battery is one that cannot easily be recharged after one use, and are discarded following discharge. Most primary cells termed dry cells utilize electrolytes that are contained within absorbent material or a separator. On the other hand, a secondary cell can be electrically recharged by passing current through the circuit in the opposite direction to the current during discharge after initial charging and discharging.

A secondary cell consists of Ni-Cd battery, Ni-MH battery, lithium ion battery and Lithium ion polymer battery [11] and the figure 1.1 is shown that there are some types of batteries. Among them, the development of lithium ion battery (LIB) is critical for advancements in a variety of applications ranging from individual electric products to hybrid electric vehicles. There are some advantages of lithium ion battery. Firstly, lithium ions have the lowest reduction potential compared as any elements and lithium ion based batteries can have the highest cell potential. Also, lithium ions as light element have one of the smallest ionic radii of any single charged ion [12]. Secondly, it has high energy density and

reactivity and also, it undergoes low self-discharge. However, it has some disadvantages that it is expensive and has a short life.

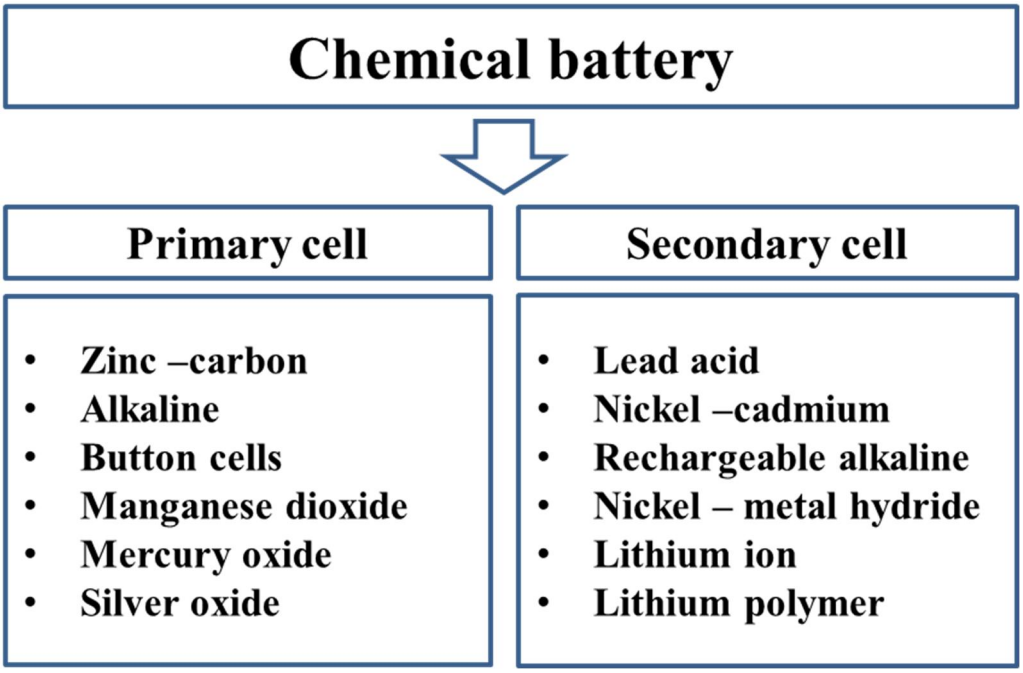

Figure 1.1 Types of primary and secondary cell.

1.1 The principle of lithium ion battery

Lithium ion batteries (LIB) largely consist of cathode, anode, electrolyte and separator. Among cathode, Cathode materials include lithium-meal oxides such as $LiCoO_2$, $LiMn_2O_4$ and $LiFePO_4$. The most common cathode material is the layered $LiCoO_2$ are the most investigated materials for LIB and this material has high stability in the high voltage range. Anode materials include mainly graphite and lithium-metal. Electrolytes offer a high mobility for lithium ions and kinds is that liquid, polymer and solid-state electrolytes and lithium ions move through highly fine pores in separator separators that are used to retain safety and stability at high temperature for LIB. The figure 1.2 is shown that

There is $LiCoO_2$/graphite as an example of basic working on during the charge/discharge process to understand the basic principle of lithium ion battery. Lithium ions have mobility between the cathode and anode with the organic solvent as electrolyte and a separator in battery system which generally operates in higher working potential than 3 V vs. Li^+/Li. Reversible intercalation and deintercalation of lithium ions from typical structures is indicated in cathode and anode [13]. During the charging process, lithium ions are deintercalated from cathode materials structure and intercalated into graphite that is anode and lithium ions are transported in reverse direction on charging process. Cathode reveals oxidation and anode reveals reduction as electrochemical reaction on discharge procedure and when the transition metal ion is reduced and accepts

one electron, lithium is oxidized to lithium cation and loses electron on discharge. On this process, batteries with circuit convert chemical potential to electrical energy by electron flow called current [14].

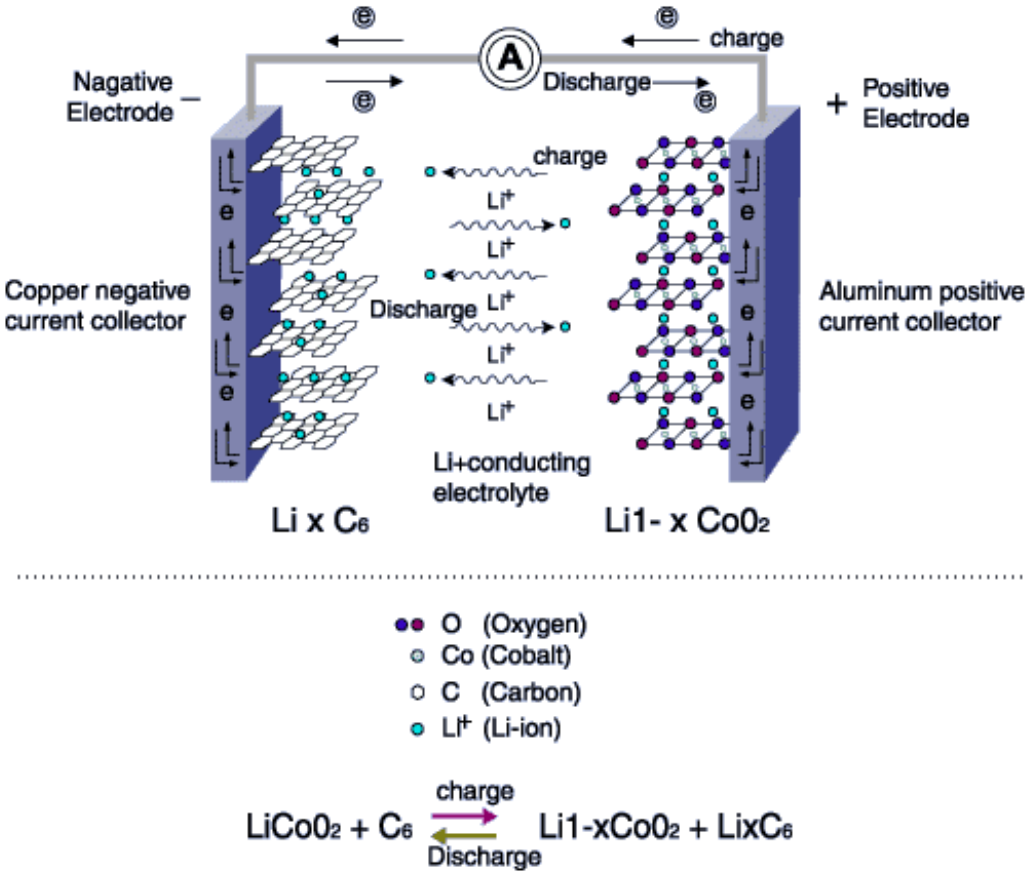

Figure 1.2 Schematic diagram of charge-discharge process of lithium ion batteries [15].

1.2 Cathode materials for lithium ion battery

Among the component of LIB, cathode is a valuable part at life cycleability, stability, reactivity and energy density and the typical cathode of LIB is composed of active materials and metal foil current collectors. The current collector acts as mechanical supports which can exist as electrode on battery and serves as electrical conductor which can connect electric energy that is made by chemical material of two electrodes into circuit. The aluminium metal foils are normally used as current collector for cathode due to their corrosion resistant caused by high oxidation state

The electrochemical performance of LIB is related in structural character of cathode material. Cathode materials are largely divided into three types as structural character. The typical cathode materials of lithium ion batteries consist of layered lithium transition metal oxides $LiMO_2$ (M = Fe, Mn, Co, Ni, Ti, V, etc.), spinel lithium transition metal oxides, poly-anion compounds such as phosphates, silicates, fluorophosphates, fluorosilicates, borates [16].

The cathode material most commonly used in lithium ion batteries is $LiCoO_2$ [16,17]. Although $LiCoO_2$ has excellent properties of charge, discharge and high specific capacity whereas cobalt has toxicity and it is more expensive than other transition metals. Also, $LiCoO_2$ is not stable as compared to other potential electrode materials which undergoes performance degradation during

overcharging [18,19]. There are several reasons have been given for the degradation during cycling. The reason is that when the electrode is delithiated during charging, cobalt is dissolved in the electrolyte [20], thus less lithium ions can be intercalated during discharge. Also, the CoO_2 layer formed after full delithiation shears from the electrode surface [21], and less capacity for lithium intercalation is caused by that reason [12].

Another $LiMn_2O_4$ is contained material of lower cost, eco-friendly and more stable than $LiCoO_2$. However, it has a lower capacity than other cathode materials. This material is that in which phase changes can occur during cycling and the capacity has been due to loss of oxygen during charging and dissolution of manganese in the electrolyte [22]. On the other hand, there are a lot of interest has been directed to phosphate cathode material as poly-anion based compounds such as olivine structured $LiMPO_4$ (M =Fe, Mn, Ni, etc.), $LiVOPO_4$ and $Li_3V_2(PO_4)_3$, which potentially allows for lower cost and high safety. A typical olivine cathode material has high stability due to strong covalent between phosphorus and oxygen atoms and it has low capacity fade after continuous cycle. So it is widely used in lithium ion batteries and these have been characterized. However, $LiFePO_4$ has low electric conductivity (10^{-9} S cm^{-1}) and lithium ion diffusion coefficient (D = 10^{-14} cm_2 s^{-1}). Also, it is suggested that olivine such as, $LiMnPO_4$, $LiCoPO_4$ and $LiNiPO_4$ does not have the excellent thermal stability compared as $LiFePO_4$.

Therefore, the relevant safety of phosphates is generally related to other poly-anion compounds which are a new material such as $Li_3V_2(PO_4)_3$ is a promising battery cathode.

The cathode material, $Li_3V_2(PO_4)_3$ with the high theoretical capacity of 197 mAh g^{-1} has appeared as new promising cathode materials due to its enhanced electrochemical properties which is high Li diffusion coefficient, discharge voltage, and energy density [23]. This $Li_3V_2(PO_4)_3$ is observed as two different phases that are monoclinic and rhombohedral structure in which the monoclinic structure is more thermodynamic stable and the rhombohedral structure indicate one plateau from one two-phase transition between $Li_3V_2(PO_4)_3$ and $Li_1V_2(PO_4)_3$ that corresponds to extraction of two lithium atoms [24]. The monoclinic structure that has all three lithium ions shows more complicated behavior from the series of two-phase transitions during lithium extraction. So, there are some advantages of monoclinic structured material are that it has high capacity and easy synthesis as a cathode material for LIBs. However, the rigid covalent bonding of larger poly-anion phosphate $(PO_4)^{3-}$ unit in (3D) framework of LVP assure the structural and thermal stability but the large poly-anion $(PO_4)^{3-}$ unit also bring some inactive mass into the electrode resulting in relatively low theoretical which lowers both the specific capacity and energy. So, the monoclinic $Li_3V_2(PO_4)_3$ has the low electronic conductivity (2×10^{-8} S cm^{-1}) to limit the wide application, several investigation to overcome this problem have been made by addition of

conductive materials [1].

For the improvements in electrochemical performance of $Li_3V_2(PO_4)_3$ (LVP), their isomorphs studies have been carried out such as surface conducting modification via coating of conducting metal oxides, various synthetic strategy, particle size reducing via formation of nanostructured materials, metal cation doping on lithium or iron sites, and anion doping at $(PO_4)^{3-}$ site to overcome these problems [25].

Considering the above mentioned issues, the evolution of borate compounds as cathode materials would be great of interest, as the $(BO_3)^{3-}$ unit is the lightest poly-anion group (M.W=58.8) among all poly-anion compounds of phosphate and silicates with larger tetrahedral $(PO_4)^{3-}$ unit (M.W=95.0) and heavier tetrahedral silicate SiO_4, could possibly increase the theoretical capacity, and energy density by approximately >1.3 times [26]. Additionally, the boron ion present in $(BO_3)^{3-}$ unit show low transition metal redox energies which requires very small amount of lithium for reversibility involving the lowest volume change (ca. 2%) during cycling. The thermodynamic study of borates compounds shows the reduction couple between 3.1 V and 2.9V /Li with higher electronic conductivity (3.9×10^{-7} S/cm) [27] better than phosphate compounds which removes the obstacles of low Li^+ diffusivity, poor intrinsic electronic conductivity, high energy barrier in lithium ion channels and Li blockage by anti-site defects as reported in phosphate compounds. Recently, the successful establishment of very

few borate based compounds of $LiFeBO_3$ [28] and $LiMnBO_3$ [29] compounds as cathode material with the superior electrochemical performance. The poly-anion compound of $Li_3M_2(BO_3)_3$ (M=Al, V, Cr, Fe, Ni and Ga) based on triangular $(BO_3)^{3-}$ unit will be the promising cathode materials and meet the stringent requirements of high theoretical capacity, wide voltage operability, high energy density, long cycle life, superior electrochemical performance for the application in hybrid electric vehicles (HEVs) and electric vehicles (EVs).

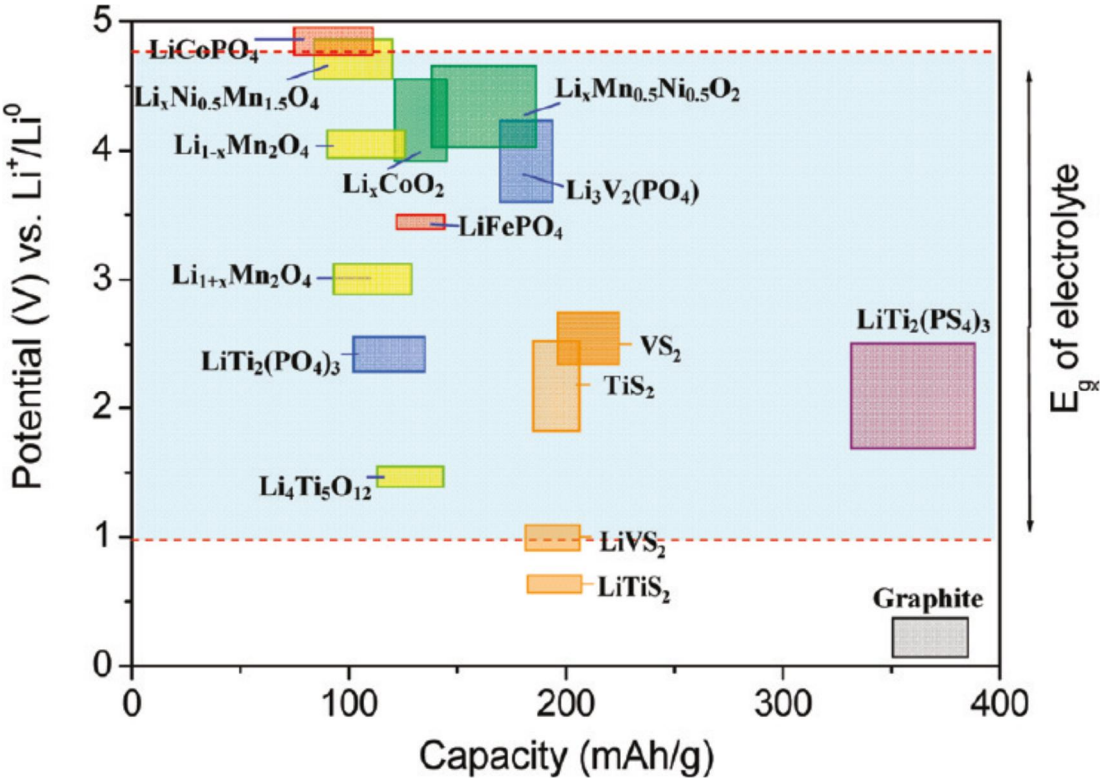

Figure 1.3 Voltage versus capacity of several electrode materials relative to the window of the electrolyte 1M $LiPF_6$ in EC/DEC (1:1) [14].

Material	**$LiCoO_2$**	**$LiMn_2O_4$**	**$LiFePO_4$**	**$Li_3V_2(PO_4)_3$**
Structure	Layered	Spinel	Olivine	Monoclinic, Rhombohedral
Potential vs. Li/Li+	3.9 V	4.1 V	3.5 V	3.8 V
Specific capacity	145 mAh g^{-1}	100 mAh g^{-1}	170 mAh g^{-1}	197 mAh g^{-1}
Specific energy	546 Wh kg^{-1}	410 Wh kg^{-1}	518 Wh kg^{-1}	550 Wh kg^{-1}

Table 1.1 The comparison of the various sorts of typical cathode material

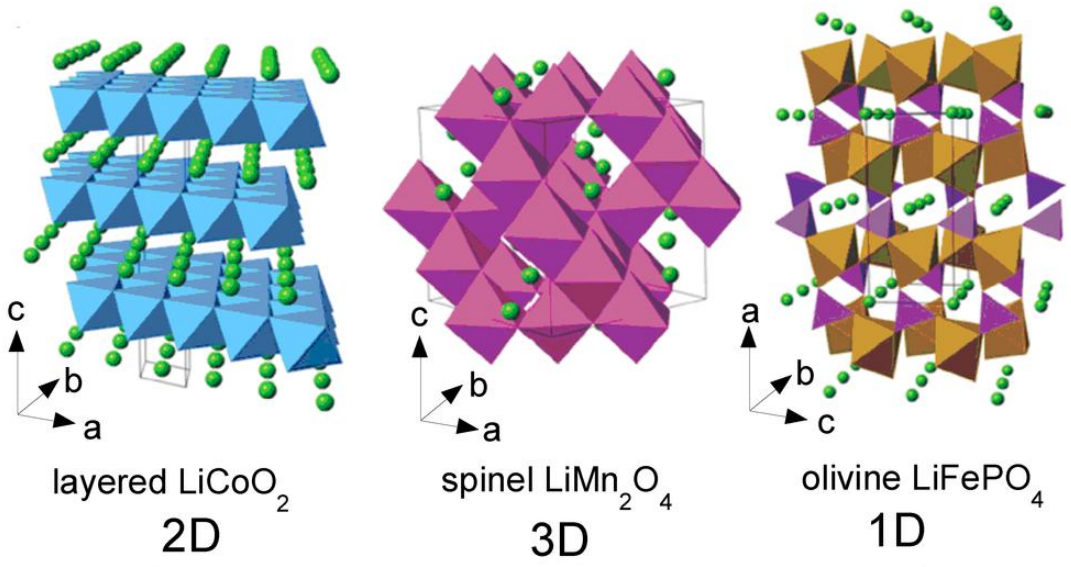

Figure 1.4 Crystal structures of the three lithium-insertion compounds in which the Li^+ ions are mobile through the 2-D (layered), 3-D (spinel) and 1-D (olivine) frameworks [30].

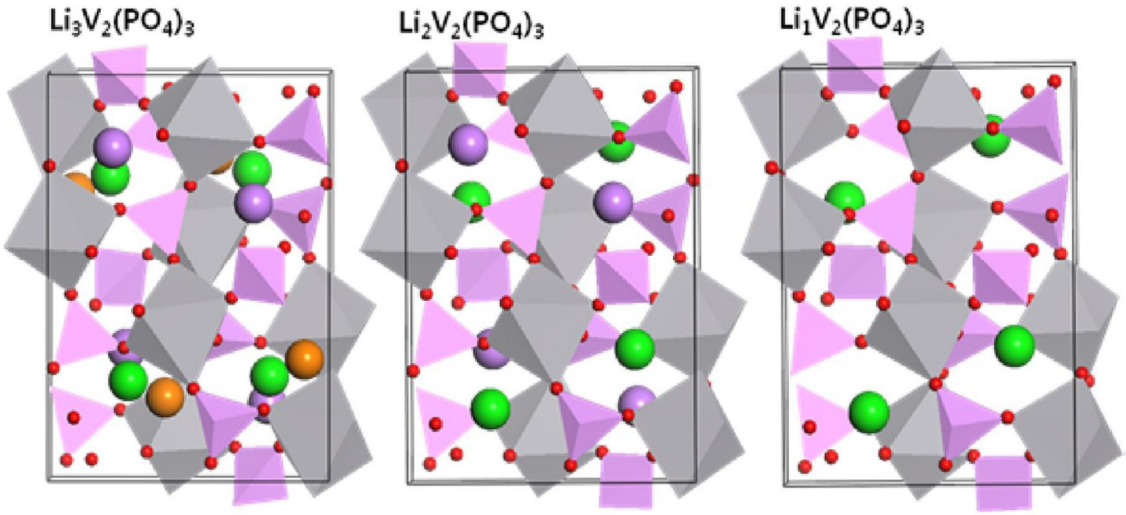

Figure 1.5 Structures of monoclinic $Li_3V_2(PO_4)_3$ (left), $Li_2V_2(PO_4)_3$ (center), and $Li_1V_2(PO_4)_3$ (right) obtained after geometry optimization, which correspond to experimentally determined structures [1].

2. Introduction of Nuclear Magnetic Resonance (NMR)

Firstly, the relationship between atoms, nuclei and molecules should be considered to understand Nuclear Magnetic Resonance (NMR). Each atom is composed of a positive charged nucleus having protons, neutrons and the nucleus is surrounded by negative charged electrons cloud. Molecules that are collections of bonded atoms are observed in a wide range of shapes and size from small compounds to larger compounds [31]. NMR is one of the well-known methods for identifying molecular structure. Also, the structure of proteins is very large, biologically important molecules for confirming the biochemical processes and these can be determined by NMR [31]. When sample is placed in a magnetic field, nuclei in the sample can absorb the specific energy at radiofrequency (RF) radiation. At that time, the nuclear magnetic resonance (NMR) can be used to observe structure of molecules. This energy at a specific resonance frequency is that depends on the strength of the magnetic field and the magnetic properties of the isotope of the atoms [32].

There are two general types of NMR spectrometers in use. Early NMR experiments were executed with a technique known as continuous wave (CW). When a constant magnetic field was maintained, the radio signal is monitored as scanning the frequency and brought each nucleus into resonance in sequence. After that, Fourier transform (FT) NMR is launched in the 1970s and this can convert signal to a frequency domain signal. At this present, FT-NMR is widely

used in various application fields.

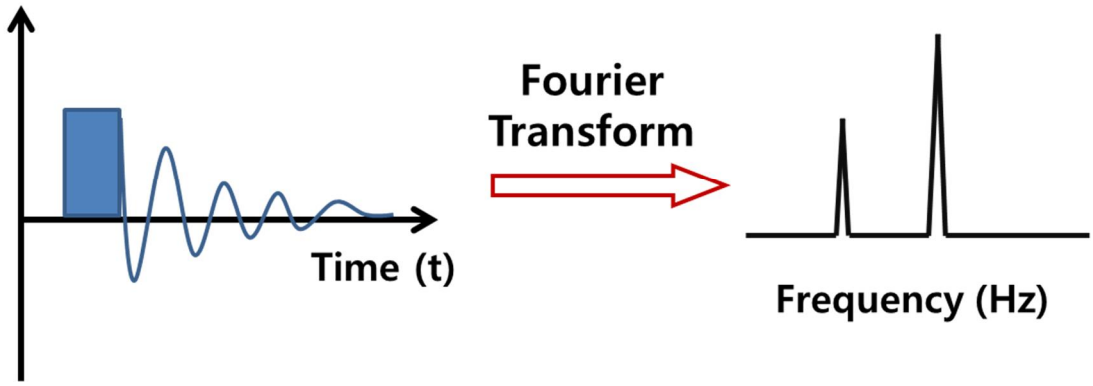

Figure 2.1 Conversion from time domain to frequency domain using Fourier transform technique.

2.1 The principle of NMR

When the energy of photon corresponds to difference in energy between ground state and excited state, electromagnetic radiation is absorbed. Nuclear Magnetic Resonance (NMR) is related in this absorption phenomenon of electromagnetic radiation in the range of radio frequency (RF). RF radiation is enough to affect to nuclear spin of atoms and the orientation of spin axis can be changed by the absorption of radiofrequency radiation in magnetic field [33].

Nuclei with spin have angular momentum that is quantized. NMR activity occurs when nuclear spin quantum number (I) is not zero and it means that only a nucleus with an even atomic mass, odd atomic number or odd atomic mass has a nuclear spin. Thus, it can be measure in NMR. In case of ^{12}C, ^{16}O is not available to measure because nuclear spin quantum number is zero and it means that the nucleus is not quantized. The angular momentum should be an integral or a half-integral since nucleus can have direction with (2I+1) discrete states. When a nucleus with a spin quantum number of 1/2 is put into external magnetic field (B_0), its magnetic moment becomes arranged in one of directions toward the field, depending on its magnetic quantum state [34]. In case of ^{1}H nucleus, it has two energy state since its nuclear spin quantum number is 1/2 (I = 1/2). Figure 2.2 illustrates that Zeeman Effect. When inserted in a magnetic field (B_0) nuclei that possess spin align themselves according to their energy states and this effect on their alignment is called the Zeeman Effect. A nucleus

with a magnetic moment in the same direction as the external magnetic field are in a low energy state and A nucleus with a magnetic moment in the opposite direction as the external magnetic field are in a high energy state.

When there is no external magnetic field, the nuclei are randomly oriented in any direction, but when a magnetic field (B_0) is applied, the nuclear spins are oriented in the same direction or in different directions. Therefore, energy becomes different. Spins in the same direction as the magnetic field (B_0) are more stable and exist in lower energy state (α) and spins in the other direction are in a higher energy state (β). The number of nuclei in each spin state can be described by the Boltzmann distribution equation demonstrated on Equation 2.1. The Boltzmann equation expresses the relationship between temperature and the related energy as shown below.

$$\frac{N_\alpha}{N_\beta} = e^{-\Delta E/kT} \qquad \text{(Equation 2.1)}$$

Where N_α is the number of spin in the higher energy state, N_β is the number of spin in the lower energy state, k is Boltzmann's constant (1.3804×10^{-23} J K^{-1}), T is the absolute temperature.

$$\Delta E = h\nu = \frac{\gamma h}{2\pi} B_0 \qquad \text{(Equation 2.2)}$$

Substituting Equation 2.2 into Equation 2.1 gives

$$\frac{N_\alpha}{N_\beta} = e^{-\left(\frac{\gamma h B_0}{2\pi kT}\right)} \qquad \text{(Equation 2.3)}$$

Where N_α and N_β represent the population of nuclei in higher and lower energy states, E is the energy difference between the two spin states, k is the Boltzmann constant (1.3805x10-23 J· K^{-1}) and *T* is the temperature in K, h is plank's constant (6.626 × 10^{-34} J·s). At room temperature, the number of spins in the lower energy level is N lower whereas the number in the upper level is N upper. Spins of nucleus with a low energy state can be excited to a higher energy state, as irradiating the nucleus with electromagnetic radiation of the correct energy. The absorption of energy occurs during this transition [35]. Thus, the signal intensity of NMR increases is related with increasing the field strength.

Isotope	Spin quantum number, I	Relative abundance in nature (%)	Gyromagnetic ratio, γ^a
^{1}H	1/2	99.98	42.5759
^{13}C	1/2	1.11	10.705
^{15}N	1/2	0.36	4.315
^{19}F	1/2	100	40.005

Table 2.1 Magnetic properties of nuclei with spin quantum number of 1/2.

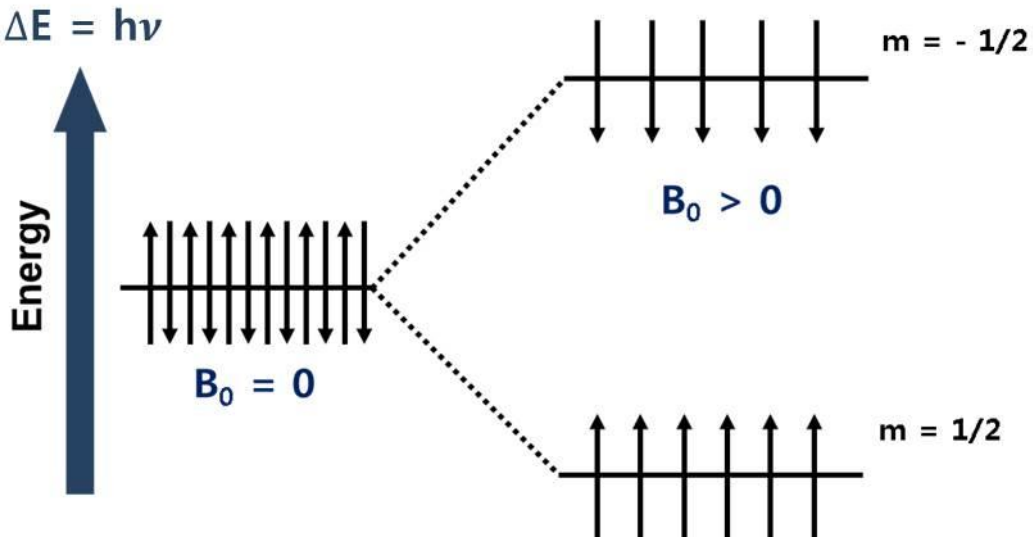

Figure 2.2 Magnetic moments and energy levels for a nucleus with a spin quantum number of 1/2.

2.2 Solid-state NMR

Solution NMR to obtain a high-resolution spectrum refers to the case where the sample is in a liquid phase, and solid NMR refers to a case where it is experimented with a solid sample. Solid-state NMR instruments can measure samples in almost all states as well as in general solids. And in contrast to liquid samples that can use low power RF pulses, solid samples can detect spin interaction using a high power RF pulse and can verify the physical properties of the sample, but exhibit a broad spectrum due to the chemical shift anisotropy, dipole-dipole coupling and quadrupole coupling.

The electrons surrounding the nucleus shield the nuclei that are affected by the magnetic field and this is local fields caused by currents of electrons that are induced by the magnetic field B_0. The electron distribution around nucleus is asymmetric and the shielding effect depends on the orientation of the molecules under the influence of the magnetic field B_0. This called as chemical sift anisotropy and the resonance frequency depends on the orientation of chemical shift tensor that is affected with magnetic field. Nuclear spins exhibit a dipole moment that interacts with the dipole moment of other nuclei and it is called as dipole coupling. The intensity of the interaction is related in the spin species, the internuclear distance, and the orientation of the vector connecting the two nuclear spins with the external magnetic field B_0. Also, an atomic nucleus with a spin greater than 1 is split by the uneven electric field due to the quadrupole

moment and energy separation by quadrupole moments does not occur in the solution state due to the symmetry. Thus, quadrupole interaction is observed only in solid-state [36].

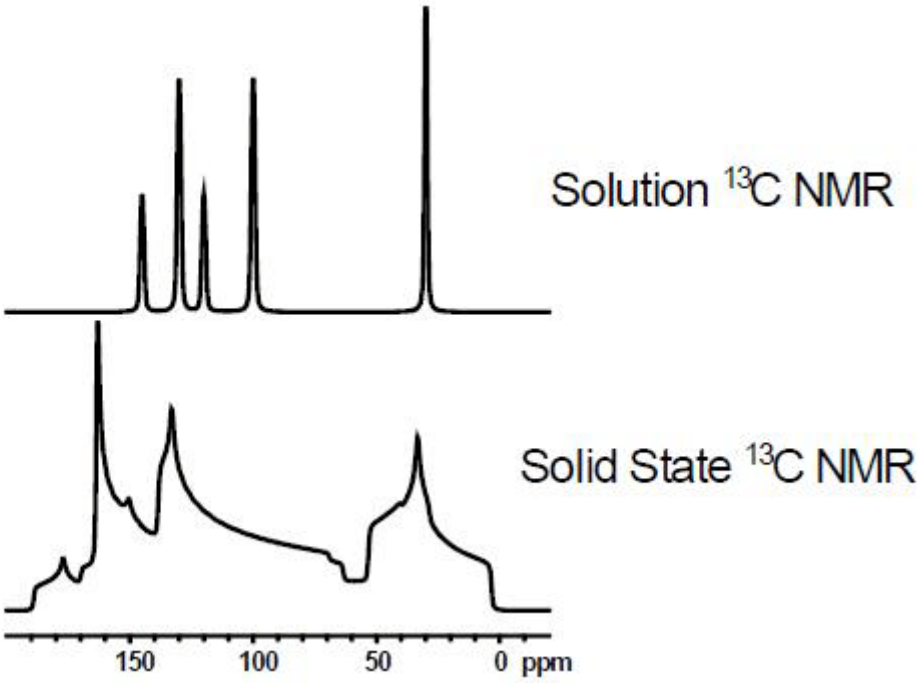

Figure 2.3 Comparison between spectra of solution ^{13}C NMR and solid state ^{13}C NMR [2].

2.2.1 Magic Angle Spinning (MAS) technique

Unlike solution NMR, which puts a sample in a tube, solid NMR rotates from several kHz to tens of kHz using a rotor. Due to fast isotropic molecular tumbling, anisotropic interactions are averaged in solution NMR. However, broad peaks are observed due to chemical shift anisotropy, dipole-dipole coupling, and quadrupole interaction in solid. The chemical shift interaction is called the chemical shift anisotropy because of the anisotropy of the electronic environment that varies depending on the direction, which is caused by the surrounding electrons that modify the local environment of the nucleus. Also, dipolar interaction occurs by direct coupling spatially between nuclei and quadrupole interaction exists when the nuclear spin I is greater than 1/2 and is caused by the interaction between electric quadrupole moment of the nuclei and the asymmetric electric field gradients surrounding the nucleus. These three interactions include in the term of $3cos^2\theta - 1$ and when they are removed, sharp peaks appear. This technique is called Magic Angle Spinning (MAS) and the expression for the term to be 0 is as follows.

$$(3cos^2\theta - 1) = 0,\ \theta = 54.75°$$

And, the sample must be spin around an axis that is oriented at 54.74° with respect to the magnetic field B_0. The spinning speed should be faster than the interaction strength to average out the anisotropy

completely.

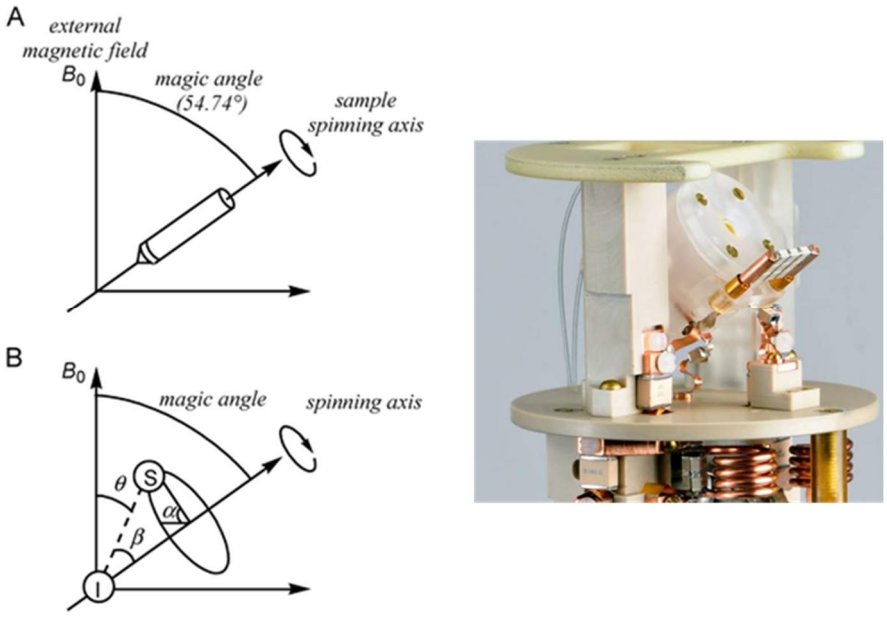

Figure 2.4 Illustration of magic angle spinning (MAS). (a) A pair of nuclear spins I and S in the solid-state NMR sample tube rotate along the axis tilted magic angle (54.741°) with respect to the external magnetic field. (b) Rotation of the I–S internuclear vector under MAS is expressed by angles a (azimuth angle; rotation of I–S vector around the spinning axis) and b (polar angle; tilt angle between the I–S vector and spinning axis) [3,4].

2.2.2 T_1 (Spin-lattice relaxation) and T_2 (Spin-spin relaxation)

In NMR, a magnetic field generated by flowing an alternating current to a coil at armor frequency is called the B_1 magnetic field. When the alternating current flowing into the coil is turned on and off, a pulse B_1 magnetic field is generated. The spin of the nucleus is aligned in the same or opposite direction to the external magnetic field along the z-axis. Since there are many nuclei oriented in the same direction as the magnetic field, net magnetization exists parallel to the external magnetic field.

At this time, the nucleus spin of the z-axis can be inverted to the x-y plane by injecting a short pulse. After the pulse injection, the spin system tries to return to equilibrium state, and the time taken for this is called the relaxation time. The relaxation time is divided into T_1 (Spin-lattice relaxation time) and T_2 (Spin-spin relaxation time) which indicates how fast the nucleus spins are magnetized in the z-axis. At equilibrium state, the net magnetization vector lies in the same direction as the external magnetic field (B_0) is called equilibrium magnetization (M_0).

When energy is applied to the system, the spin system is saturated and M_z becomes zero ($M_z = 0$). In this saturation state, the time that it takes for M_z to return to its original equilibrium state is called T_1 (spin-lattice relaxation time) and is expressed with the following equation and expressed as figure 2.5.

$$M_z = M_0 (1-e^{-t}/T_1) \qquad \text{(Equation 2.4)}$$

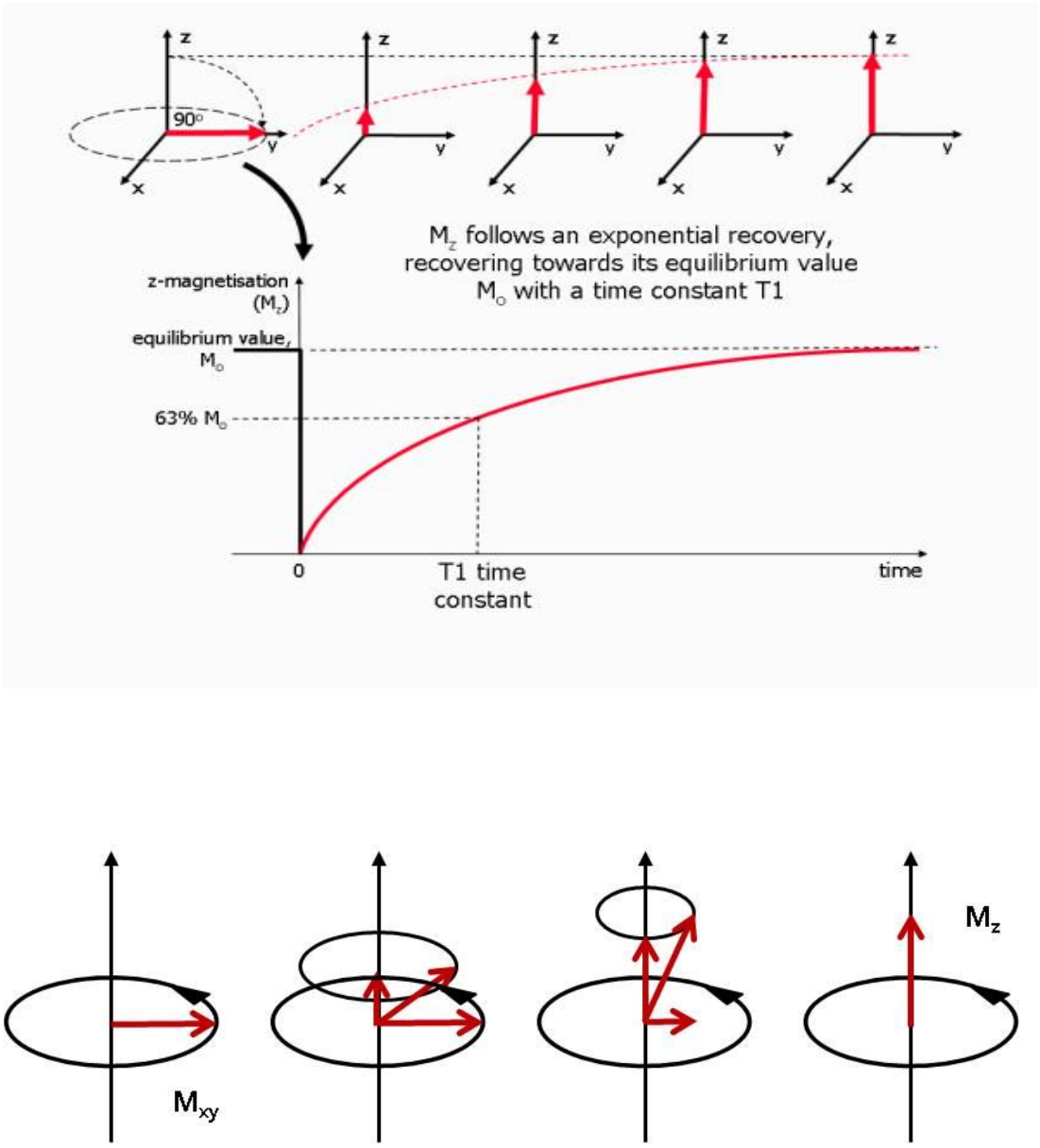

Figure 2.5 Spin-lattice relaxation (T_1) processes [5].

When the net magnetization lies in the x-y plane by a pulse, it rotates about the z-axis at the larmor frequency. The spinning motion is called precession. Precession and net magnetization experience slightly different magnetic fields in each spins, and eventually rotate at different larmor frequencies and dephasing begins to occur. As a result, a larger dephasing occurs over time. The time required for the transverse magnetization M_{xy} to return to the equilibrium state is referred to as T2 (spin-spin relaxation time) and is represented by the following equation and expressed in figure 2.6.

$$M_{xy} = M_{xyo}\ e^{-t/T_2} \qquad \text{(Equation 2.4)}$$

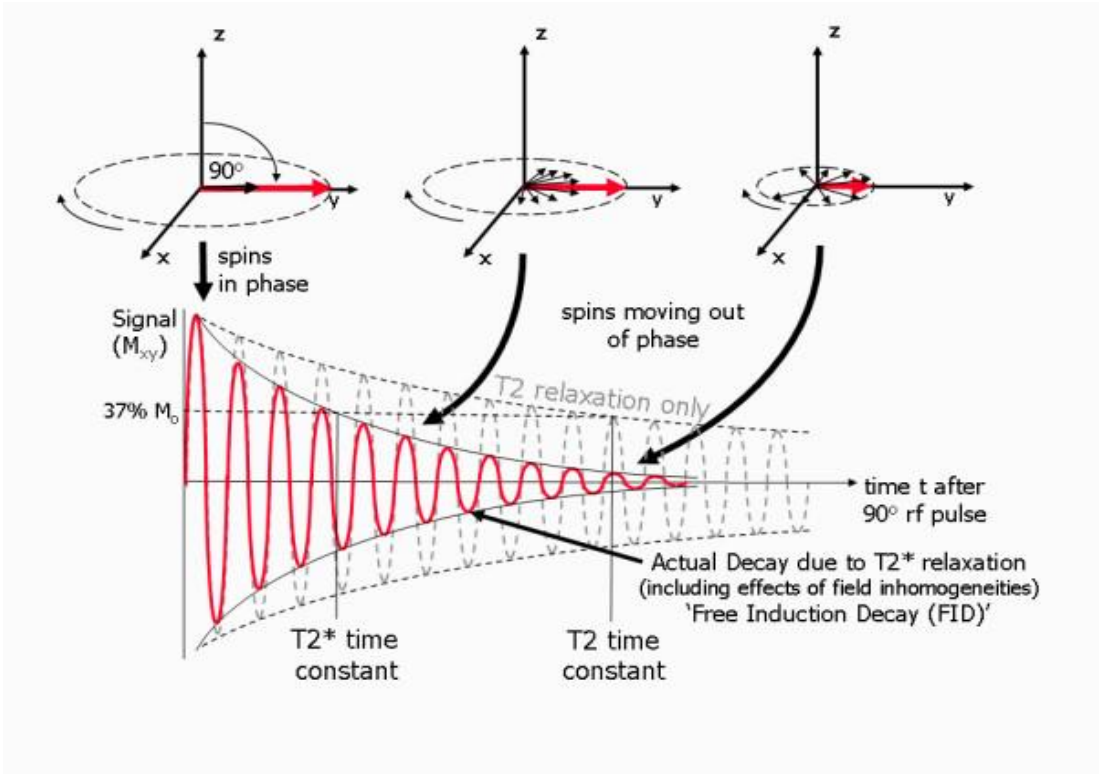

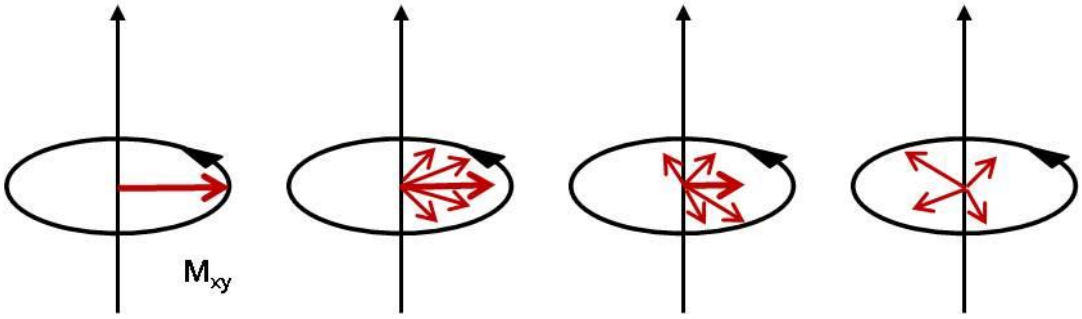

Figure 2.6 Transverse (T_2 and T_2*) relaxation processes [5].

That is, T_1 is the time for how fast the nuclear spins are magnetized in the z-axis, T_2 is how fast the magnetization is lost in the x-y plane, and T_2 is equal to or less than T_1.

2.2.3 Spin echo pulse sequence (Hahn echo)

A radio pulse excites a relaxing nucleus while acquiring a signal. The signal is obtained by decreasing the dephasing after the net magnetization vector carries out a precession about the z-axis. At this time, a sine curve is obtained with exponential decay, which is called free induction decay (FID). The most commonly used pulses in NMR are 90° pulses and 180° pulses. The 90° pulse maximizes the signal to the x-y plane where the NMR signal can detect net magnetization in the z-axis. On the other hand, a 180° pulse reverses the density of the spin, although the NMR signal cannot be detected. The pulse sequence of 1D NMR is shown as follows.

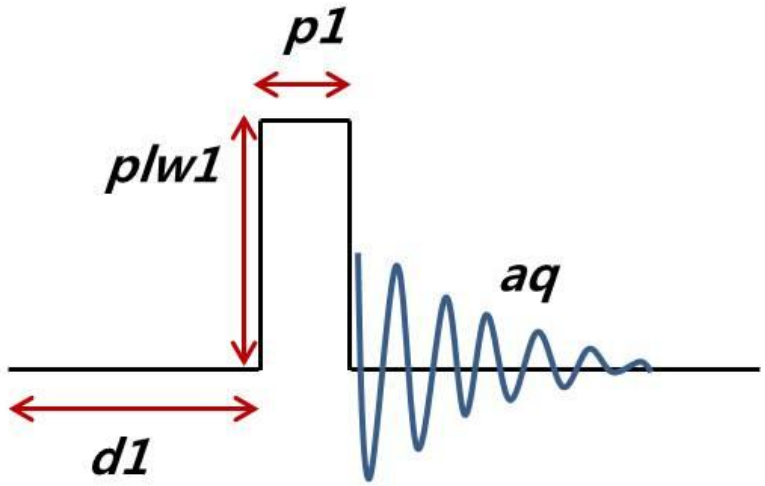

Figure 2.7 Schematic illustration of 1D NMR pulse sequence. (p1 = pulse width or duration, plw1 = RF field strength, aq = acquisition time and d1 = delay time)

The parameters of spectrometer frequency, pulse width (pw), recycle delay (d1) and acquisition time (aq) are important to obtain NMR signals. The spectrometer frequency is a specific frequency of a radio wave pulse which depends on the strength of the magnetic field and the type of nucleus to be measured. The pulse width is the amount of time of the pulse energy applied to a particular sample to invert the spin in the x-y plane and depends on the power or attenuation of the pulse. The recycle delay (d1) appears at the beginning of the pulse sequence and is the time it takes for the spin to completely magnetize in the z-axis, also called delay time. After the radio wave pulse is applied, the nuclear spins do not immediately return to equilibrium and relaxes with time constant T_1. This depends on factors such as the nuclear environment, temperature, solvent, and other magnetic field conditions. Without sufficient relaxation time between pulses, the signal is reduced and integration is not accurate. The specific time to obtain the FID is called acquisition time. If it is too long, the noise becomes large. If it is too short, a peak not related to the actual signal is observed [37].

The spin-echo pulse sequence in one of the pulse sequences most commonly used in NMR is intended to reduce any uneven effects due to spin relaxation and precession at different speeds in the sample. In solid NMR, it is mainly used for short T_2. After applying a 90° pulse, apply a 180° pulse and rotate the magnetization 180° about the x'-axis. This is for preventing the loss of

magnetization by applying a 180° pulse, which is an inversion pulse with a non-uniform phase of zero [38]. After a 90° pulse is applied, a 180° pulse is applied after a short time of τ and another time of τ, which is the same time that causes a spin echo signal. The signal thus obtained is called echo, not FID.

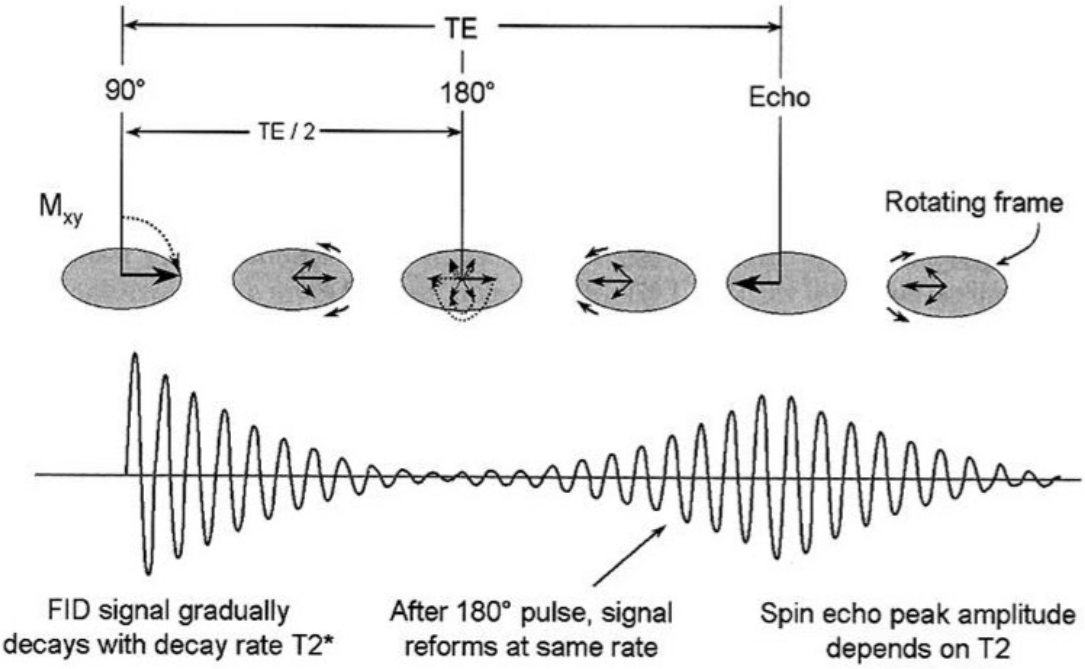

Figure 2.8 The spin-echo pulse sequence [6].

2.2.4 Structural analysis using NMR for cathode materials

It is important to study structure measurement around lithium ion and the location and migration path of lithium ion among development factors of lithium ion battery.

Solid-state NMR is useful for analyzing the bonding structure between lithium ions and transition metal oxides in a cathode material. The NMR spectra are heavily influenced by the electrical structure of the material, and it is possible to distinguish between diamagnetism and paramagnetism. Structural analysis is made mainly for pure materials, and it is possible to check how the structure of the local structure changes after several charges and discharges. As nuclear spins of ^{6}Li and ^{7}Li have more than one in solid-state NMR, the Li MAS NMR spectrum of the battery material is affected by large interactions including quadrupole coupling and interaction with unpaired electrons in paramagnetic samples. As a result, the signals can be very complex, but using the previously described MAS NMR, high resolution signals can be obtained by rotating the sample at a high spinning rate.

In the case of LiM_2O_4, which is a material of the spinel structure synthesized at 700 ° C, the manganese ion retains the spinel host framework as a whole while circulating from LiM_2O_4 to MnO_4, a large hyperfine shift of 500 ppm or more is confirmed from the chemical shift range of a typical lithium

containing diamagnetic compound in the ^{6}Li and ^{7}Li MAS NMR spectra. Also, this material is a mixture containing both Mn^{3+} and Mn^{4+} ions and is a hopping semiconductor that occurs between e_g orbitals of manganese ions. Since this hopping time scale is faster than the NMR time scale, it appears that the spin of lithium is averaged to a manganese oxidation state of $Mn^{3.5+}$ and appears as one on the NMR signal.

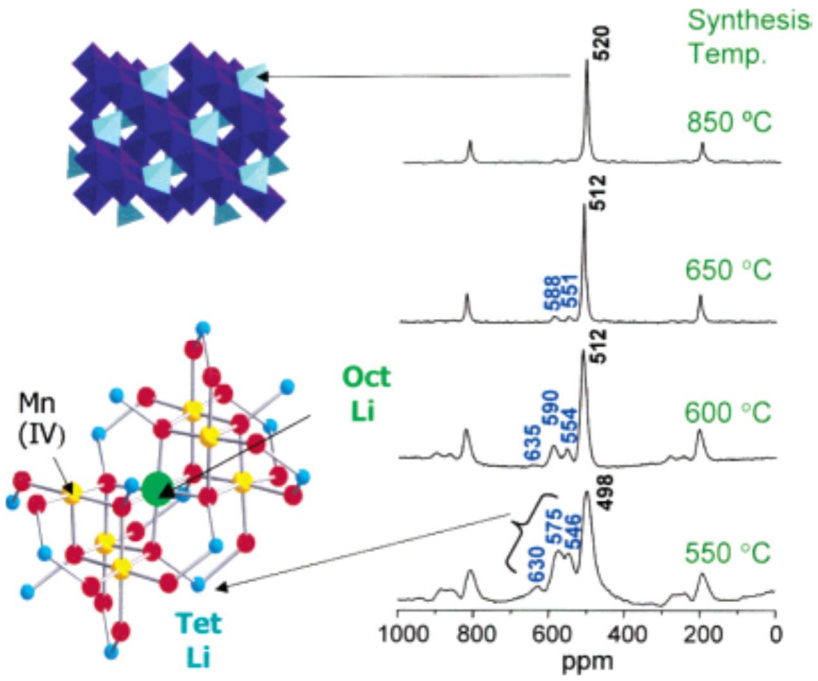

Figure 2.9 ^{6}Li MAS NMR spectra of the spinel $LiMn_2O_4$ based on sintering temperature [7]

In the case of $LiCoO_2$ related materials, the NMR spectra show the oxidation of Co^{3+} and doped ions, as well as changes in the electronic conductivity of these materials. This is because the NMR spectra are very sensitive to the semiconductor to transition metal phase transition. Low-spin Co^{3+} ions are normally diamagnetic, but they exhibit very poor paramagnetism for layered $LiCoO_2$ which is temperature-independent. Mainly, the ^{6}Li and ^{7}Li MAS NMR spectra on $LicoO_2$ are all found at -0.2 ppm, consistent with the presence of essentially spinel localized environments and low-spin Co^{3+} ions.

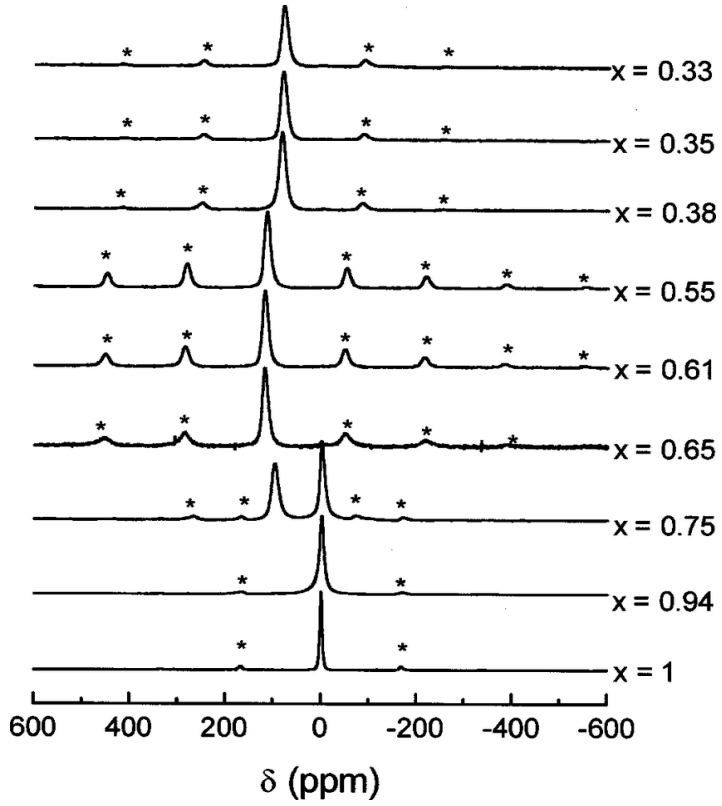

Figure 2.10 ^{7}Li MAS NMR spectra of various Li_xCoO_2 (0.33< x <1) deintercalated phases recorded with a single-pulse sequence at 13 kHz spinning speed and the spinning sidebands are marked with asterisks (*) [8].

In the case of an olivine structure such as $LiFePO_4$, $LiMnPO_4$, and $LiNiPO_4$, a single resonance with a spinning sideband was observed for all compounds indicating the presence of a localized environment in the lithium cation and a very small range of shift of -90 to 70 ppm relative to the spinel structure appear. This is called the inductive effect of the phosphate group and it is expected that the covalent bond of P-O increases the ionic character of the Li-O and M-O bonds, thereby reducing the overlap and hence the degree of hyperfine interactions in these materials.

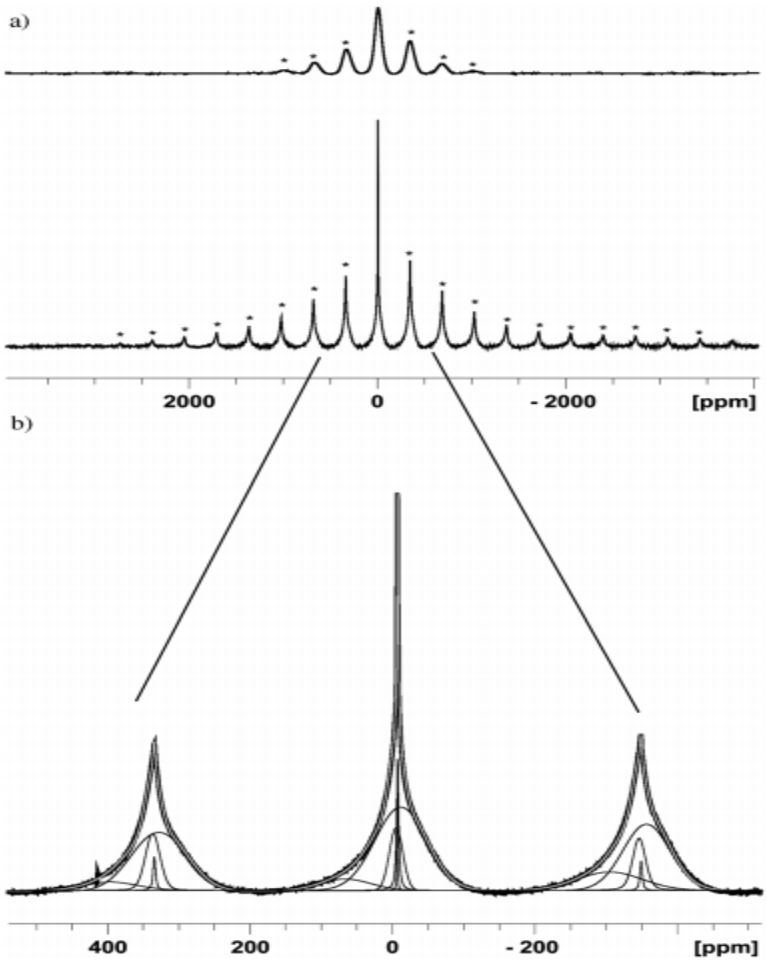

Figure 2.11 (a) ^{7}Li MAS NMR spectra of $LiFePO_4$ (1^{st}) and biphasic $Li_{0.5}FePO_4$ ($0.5LiFePO_4$:$0.5FePO_4$) (2^{nd}). (b) Deconvolution of biphasic $Li_{0.5}FePO_4$ with MAS = 40 kHz and the spinning sidebands are marked with asterisks (*) [9]

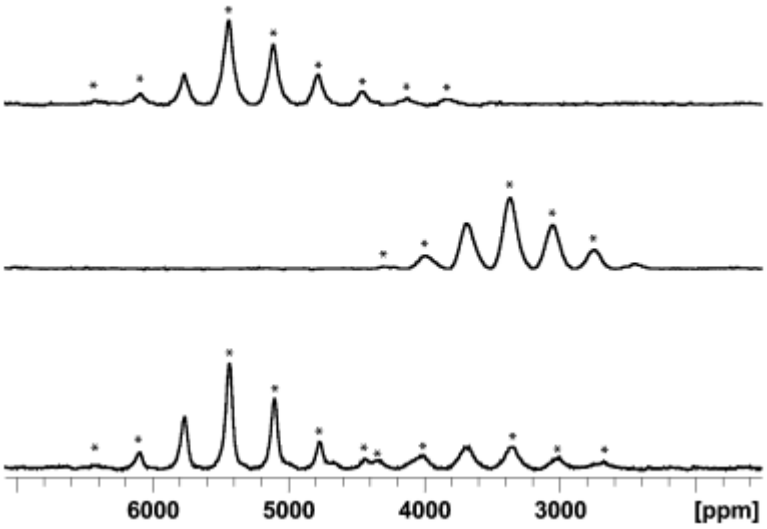

Figure 2.12 ^{31}P MAS NMR of $FePO_4$ (top), $LiFePO_4$ (middle) and biphasic $Li_{0.5}FePO_4$ (bottom) all at room temperature. Isotropic shifts for $FePO_4$, $LiFePO_4$ are found at 5800 and 3800 ppm respectively and the spinning sidebands are marked with asterisks (*) [9].

3. Experimental

3.1 Synthesis of cathode material using combustion method

The highly porous nanostructured $Li_3V_2(BO_3)_3$/C was prepared by using the analytical grade chemicals with a stoichiometric amount of lithium nitrate, $LiNO_3$ (99.99%, Sigma Aldrich), ammonium metavanadate, NH_4VO_3(99.0%, Alfa Aesar) and boric acid, H_3BO_3 (99.5%, Kanto) were dissolved in distilled water. The stoichiometric amount of citric acid (99.5%, Junsei) (2:1) was added to the solution. The color of orange solution was heated on a hot plate using a magnetic stirrer at about 80°C to evaporate the water and after 3hr, a foam-like navy coloured gel is formed which emitted the large volume of gases and then it was produced a fluffy precursor powder within few minute, due to the exothermic reaction between the metal nitrates and the oxidant fuel. The obtained precursor was grounded and precalcined at 350 °C for 3 h followed calcined at 450 °C for 5 h under argon atmosphere in electrical furnace.

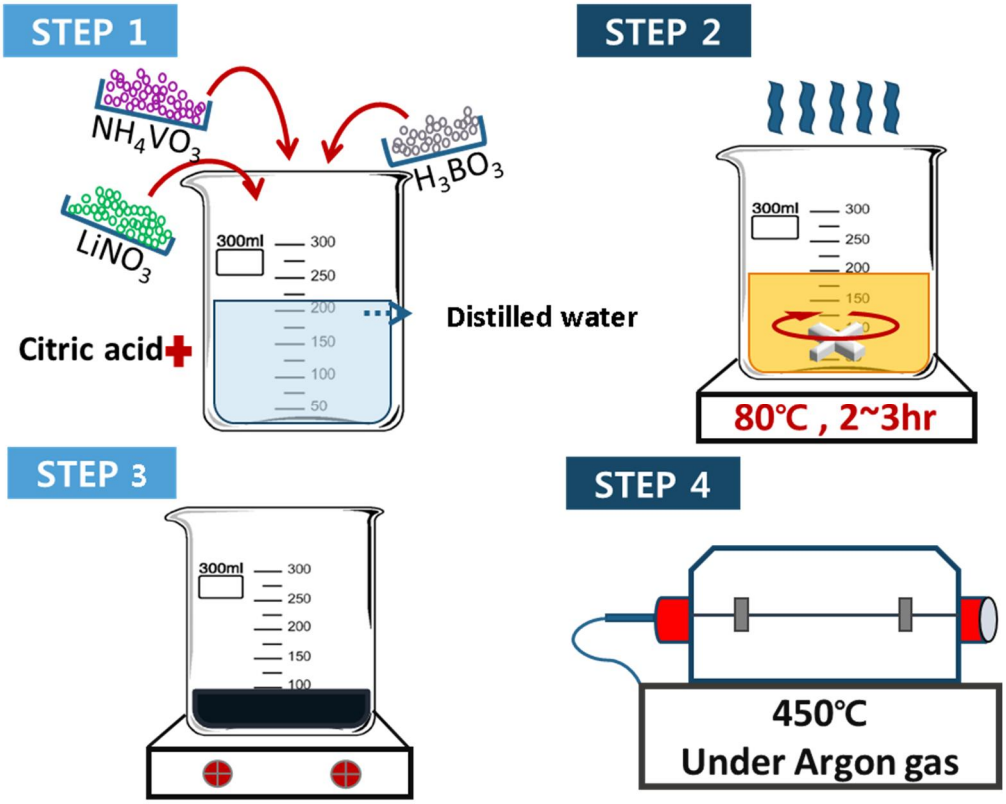

Figure 3.1 Illustration of synthetic procedures of $Li_3V_2(BO_3)_3$/C as cathode material.

3.2 General characterization of cathode materials

X-ray diffraction (XRD) patterns of the annealed cathode materials were measured by using a Rigaku Ultima 4 diffractometer with Cu K_α radiation (λ = 1.5406 Å). The surface morphology and grain sizes of the prepared cathode materials were identified by JEOL JSM-6500F field emission scanning electron microscope (FE-SEM). Transmission electron microscope (TEM) image were acquired by Hitachi H-8100 TEM. XPS analyses of $Li_3V_2(BO_3)_3$/C were performed using a Thermo Fisher K-Alpha in wide scan survey mode and high-energy resolution. Elemental quantification and chemical state assessment were obtained by full K-alpha evaluation.

3.3 Electrochemical test of cathode materials

For the electrochemical characterization, electrodes were fabricated using the synthesized cathode materials. The slurry was prepared by mixing active material, conductive material (super-P) and Polyvinylidene fluoride (PVDF, Aldrich, M_w = 534,000) used as a binder with N-methyl pyrrolidone (NMP) at a weight ratio (wt.%) of 80: 10: 10 for electrode fabrication. and the resulting slurry was pasted on aluminum foil for current collector and dried in a vacuum oven at 90 °C for 2 hr. After that, they were squeezed using a roll press for uniformity of the electrode thickness and then, the electrode with active material was assembled into 2016 coin cells in an argon-filled glove box. Non-aqueous 1.15 M $LiPF_6$ in EC/DMC/DEC (ethylene carbonate/dimethyl carbonate/diethyl carbonate) with a volume ratio of a 3:4:3 was used as the electrolyte. The cell were charged and discharged over a voltage range from 1.0 to 4.5 V versus Li/Li^+ electrode and electrochemical cycle tests and cyclic voltammetry (CV) were performed at a scan rate of 0.05mV/s using a galvanostatic automatic battery cycler (WonATech WBCS3000, Korea) at ambient temperature.

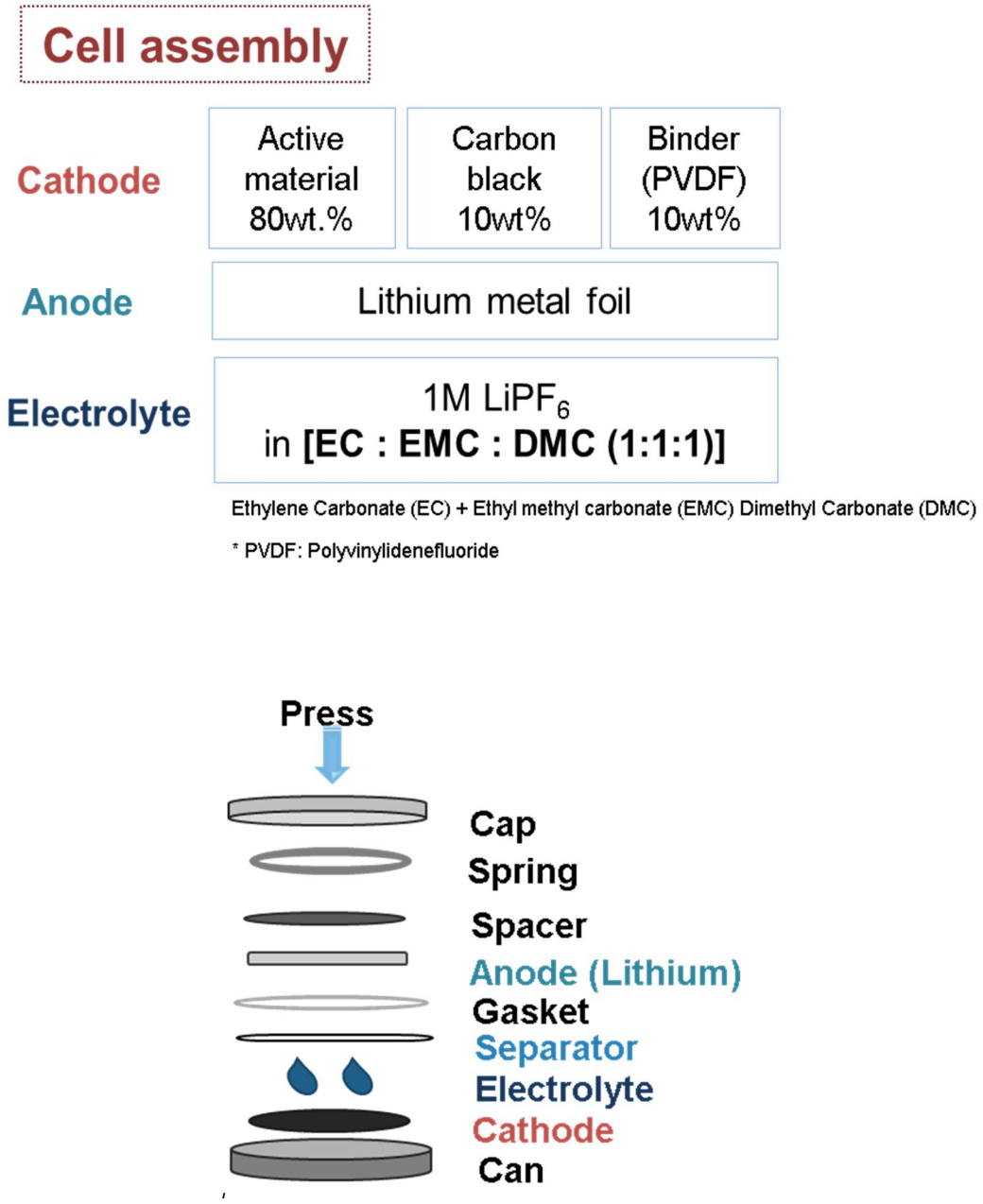

Figure 3.2 Illustration of synthetic cathode and coin cell assembly of $Li_3V_2(BO_3)_3$ /C as cathode material.

3.4 Solid-state MAS NMR study of cathode materials

^{7}Li and ^{51}V MAS NMR were measured by using a Bruker Avance Ⅲ 300 with a 7.04 T magnet at room temperature. For the MAS NMR experiments, a 2.5 mm MAS probe was used at 116.64 MHz for ^{7}Li and 78.94 MHz for a ^{51}V resonance frequency with zirconia rotor. The ^{7}Li NMR spectrum was referenced to the external 1M LiCl and ^{51}V NMR spectrum to the powder of V_2O_5. The single pulse for ^{7}Li and ^{51}V were used to observe the NMR signal and the sample spinning rate was 25 kHz, 20 kHz about each ^{7}Li and ^{51}V. The ^{7}Li spectra were acquired with a 90° pulse length of 1.4 μs, repetition delay of 2 s, 256 transients, and spectral width of 0.23 MHz. For ^{51}V NMR, the 90° pulse length of 1.5 μs, repetition delay of 1 s, and 1K transients with spectral width of 0.24 MHz were used.

Figure 3.3 Bruker Avance Ⅲ 300MHz NMR.

Figure 3.4 NMR tube and spinner.

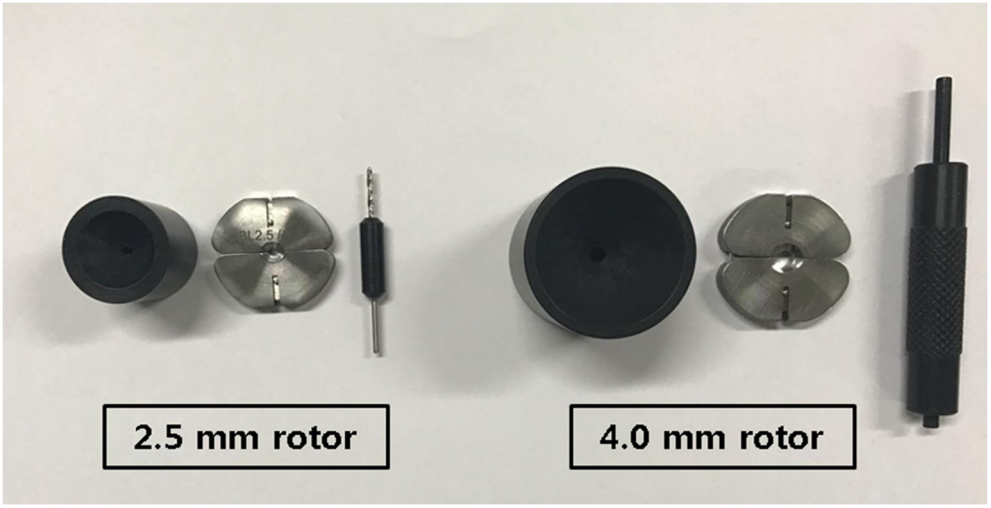

Figure 3.5 Sampling kit for solid-state NMR.

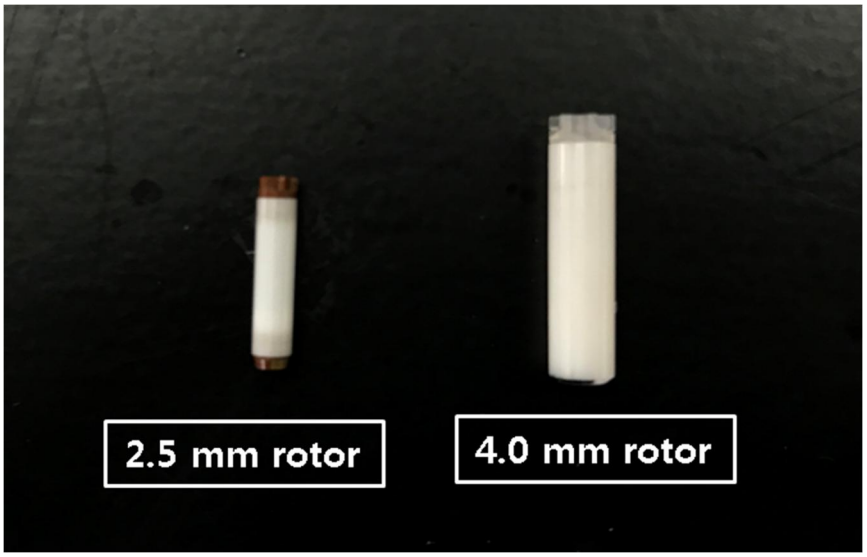

Figure 3.6 2.5 mm and 4.0 mm rotor for solid sample container.

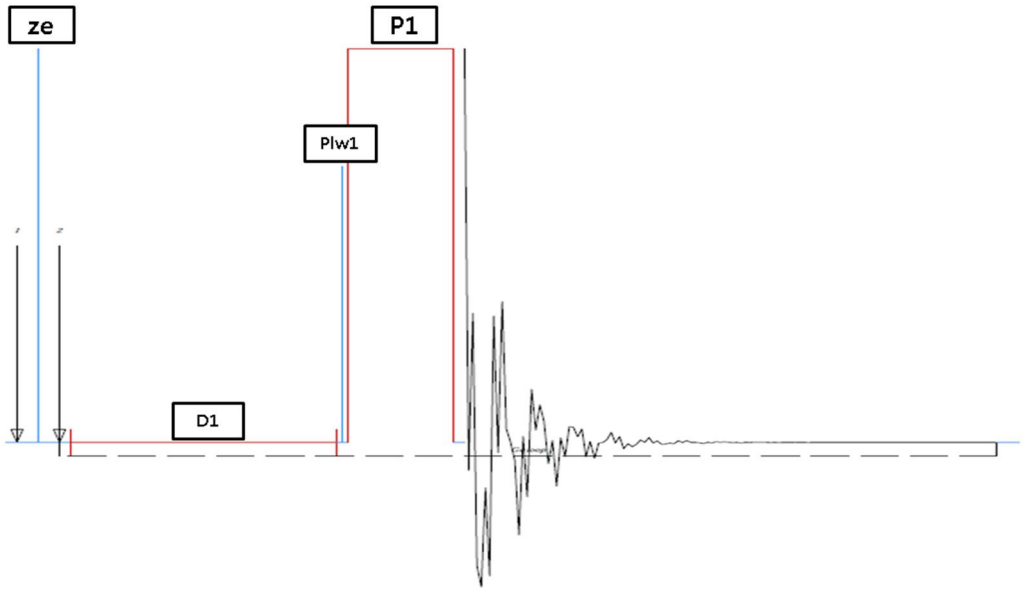

Figure 3.7 One-pulse (single pulse) parameter.

4. Results and Discussion

4.1 General characterization of cathode materials

4.1.1 X-ray Diffraction (XRD) for structural characterization

XRD is useful for determining the crystal structure of a solid sample by measuring the diffraction according to the angle change of the X-ray irradiating the sample. This material is measured at different sintering temperatures of 450℃, 500℃, 550℃ and 600℃, respectively. Figure 4.2 shows the XRD pattern of $Li_3V_2(BO_3)_3$/C sintered at 450°C for 5hr due to the simplest phase. The observed XRD profile clearly indicates the formation of mixed phase of orthorhombic LiV_2O_5 phase (01-074-0055) (space group P21/m)[39] with minor phase of monoclinic $LiVO_3$ (JCPDS Card no.: (00-039-0378), space group: C2/c)[40] and dilithium tetraborate (01-084-2191, $Li_2B_4O_7$).

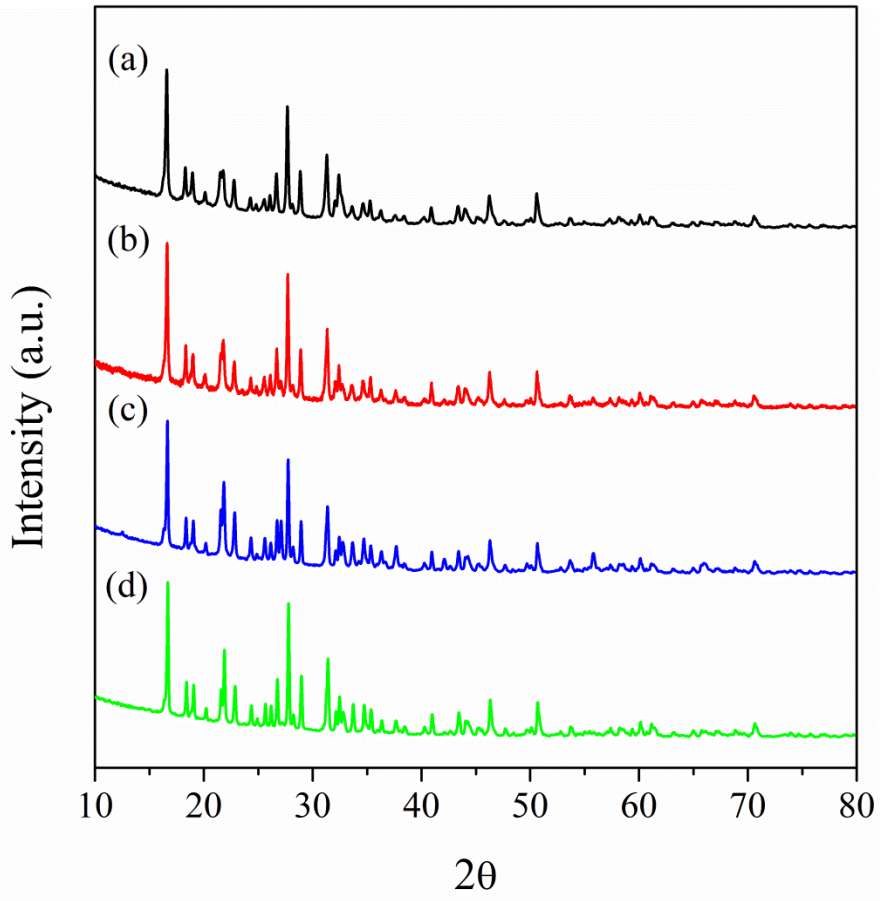

Figure 4.1 The XRD patterns of $Li_3V_2(BO_3)_3$/C sintered at each temperature. (a) 450℃, (b) 500℃, (c) 550℃ and (d) 600℃.

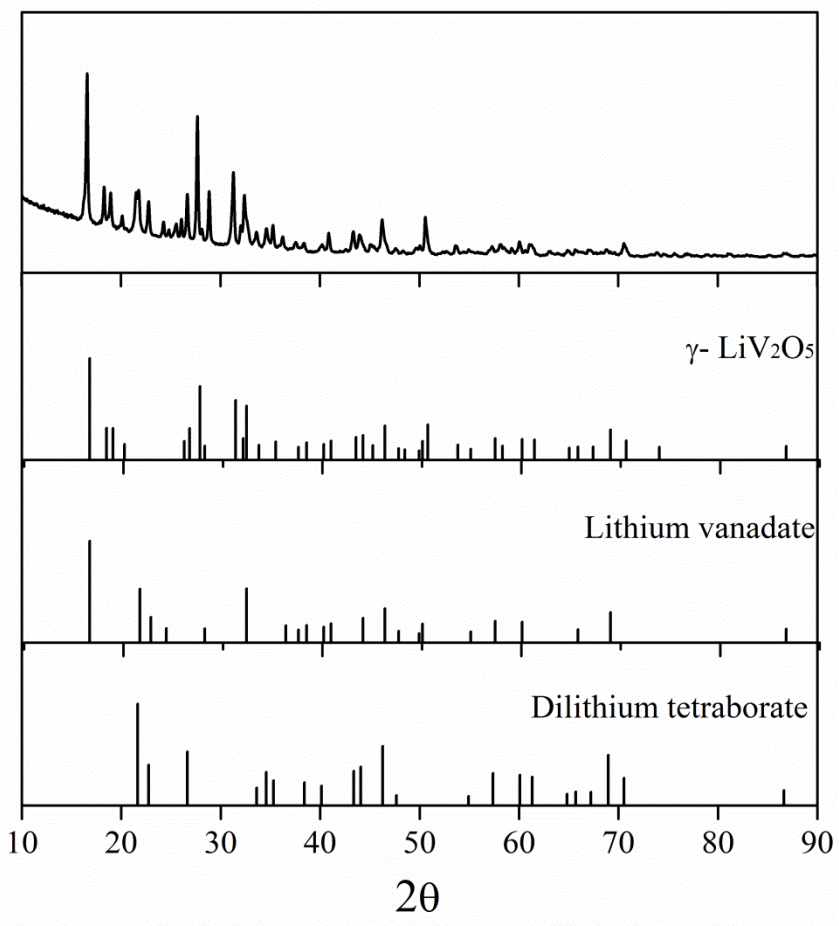

Figure 4.2 The XRD patterns of $Li_3V_2(BO_3)_3$/C sintered at 450℃.

4.1.2 Scanning Electron Microscopy (FE-SEM) and Transmission Electron Microscopy (HR-TEM) analysis for particle size and morphology

SEM images were recorded (Figure 4.3(a,b)) at low and high magnification to analyze the morphology of the $Li_3V_2(BO_3)_3$/C. This material showed the rough and sponge-like appearance of the grains which are mainly composed of micro sized grains and messy large pores with diameter in the range of 0.5 -3 μm. The novel microporous morphology is more suitable and effective for electrolyte to permeate into the inside of the electrode which is profitable to the high performance of the $Li_3V_2(BO_3)_3$/C [41].

Also, to determine the lattice and morphology of the particles, the particle shape was measured using HR-TEM. As shown in the figure, (c) shows a particle shape similar to that observed in the SEM image and confirmed the pore size of 95.47nm size.

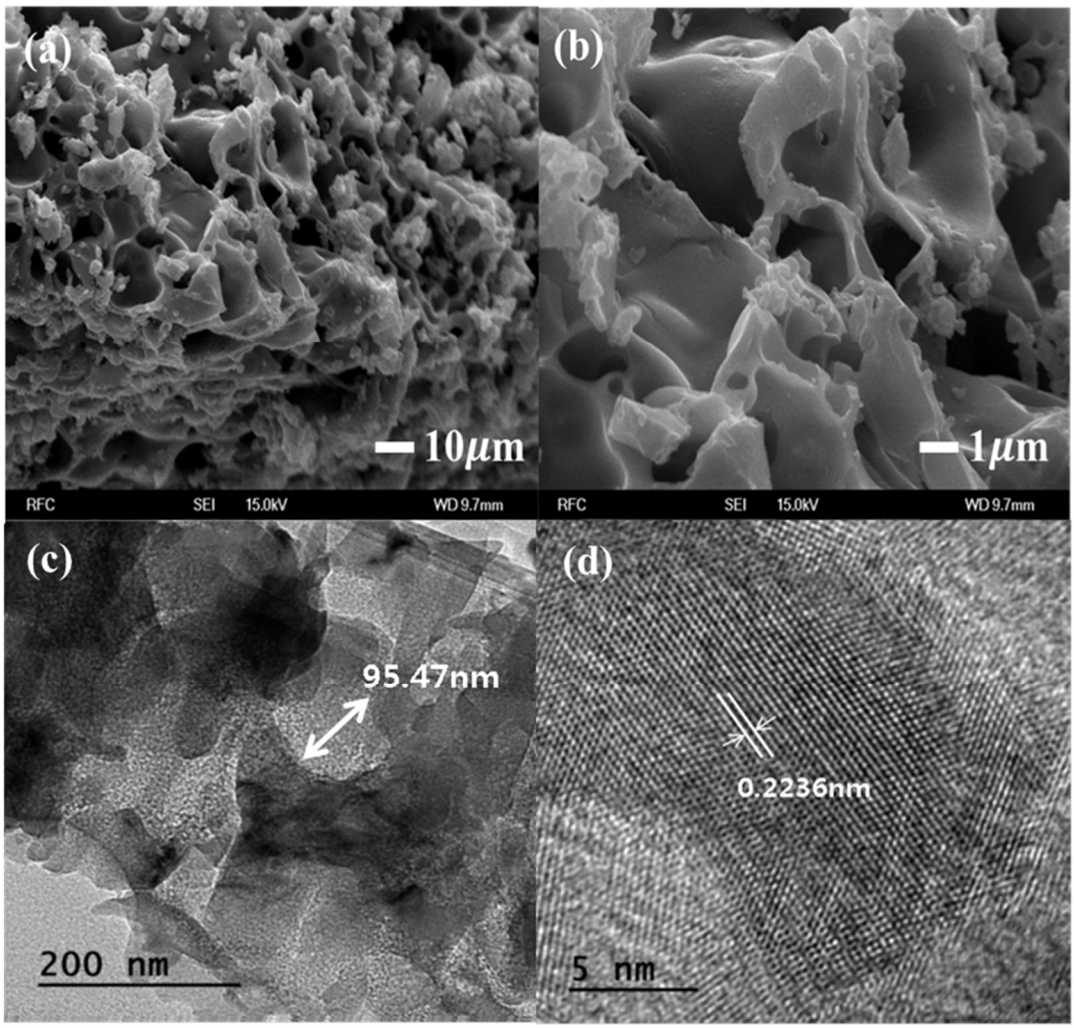

Figure 4.3 SEM images for (a) low magnification, (b) high magnification, (c) TEM image and (d) HR-TEM image of $Li_3V_2(BO_3)_3$/C.

4.1.4 X-ray photoelectron spectroscopy (XPS) analysis for oxidation state of cathode material

XPS analyses were carried out to investigate the chemical composition and oxidation state of the metal ions Li, V, and B in $Li_3V_2(BO_3)_3$/C. Figure 4.4(a) presents the XPS survey spectra of $Li_3V_2(BO_3)_3$/C which clearly reveals the peaks of Li, V, B, C and O. Figure 4.4(b,c) display the XPS spectra of Li1s and B1s appears as a single peak with the binding energy (BE) 55.5 eV and 192.4 eV respectively. The BE values of Li1s and B1s are consistent with +1 oxidation state of Li in $LiFePO_4$ as reported earlier [42,43] and +3 oxidation state of B in pure B_2O_3 [44]. Figure 4.4(d) shows that fitting of the V2p core level spectra using a Gaussian Lorentzian fits in to two peaks at 517.3 eV and 524.6 eV which is assigned to the $V2p_{1/2}$ and $V2p_{3/2}$. It was found that the binding energy for the $V2p_{1/2}$ and $V2p_{3/2}$ peaks are well matched with the BE values those measured in $LiVOPO_4$ for the V^{4+} [45]. Figure 4.4(e) showed the C1s peak with a binding energy of 285 eV exist in the spectra which suggests that the citrate was decomposed into carbon during calcination, and residual carbon exists in $Li_3V_2(BO_3)_3$/C [46] while the C1s peak at 289 eV for C-O is absent used for the calibration of instrument. This is profitable to increase the electronic conductivity for $Li_3V_2(BO_3)_3$/C. The O1s peak located at 531.9 eV as shown in figure 4.4(f) which is well agreement with the BEs of reported for O1s peak in $LiFeBO_3$ and $LiFePO_4$ [45,47]. Hence it can be concluded that the oxidation state of Li, V, and B

in $Li_3V_2(BO_3)_3$/C are +1, +4 and +3, respectively.

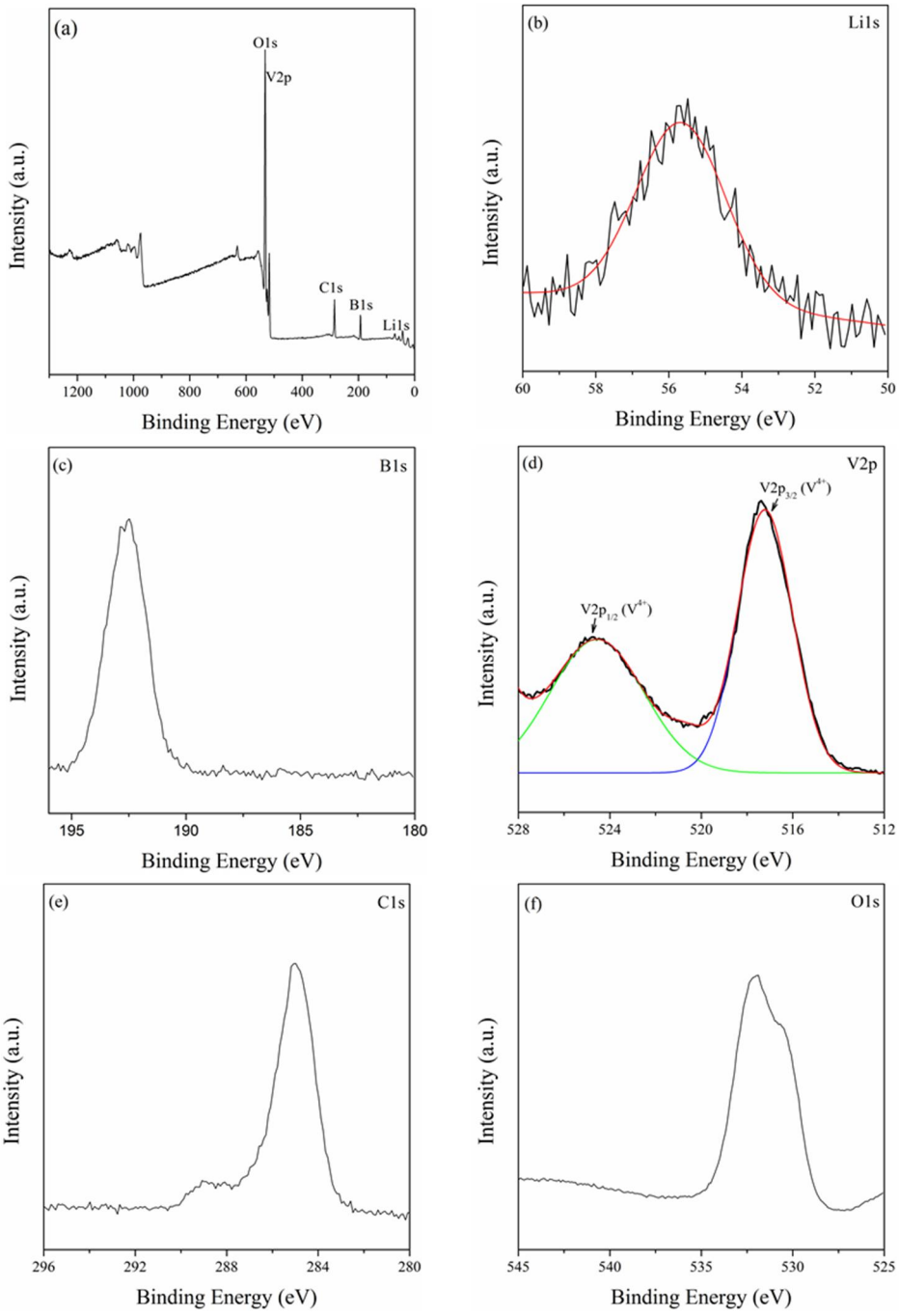

Figure 4.4 The XPS graph of $Li_3V_2(BO_3)_3$/C. (a) Survey spectrum, (b) Lithium, (c) Boron, (d) Vanadium, (e) Carbon, (f) Oxygen peak.

4.2 Electrochemical study of synthesized cathode materials

4.2.1 Charge-discharge properties, long cycle performances, cycling profiles

The electrochemical performance of the $Li_3V_2(BO_3)_3$/C are shown in figure 4.5. In figure 4.5(a), the initial charge curve at 0.05 C rate shows the electrochemical behavior in the voltage range of 2.5-4.5 V with specific charge capacity of 67.4 mAh g^{-1} and is followed constant voltage plateau with capacity of 81.3 mAh g^{-1}, while the initial discharge curve shows the wide voltage range electrochemical behavior in the voltage range of 0.9-4.5 V with an exceptionally high discharge capacity of 257 mAh g^{-1} approaches to 95.6% of its theoretical capacity (268.7 mAh g^{-1}). The discharge curve of LVB/C shows three step discontinuous discharge plateau and showed the dissimilar behavior from the phosphate materials ($LiMPO_4$, M=Fe, Mn, Co) where they showed a single continuous discharge plateau due to the removable single lithium ions possess the equivalent sites that indicate the same site energy while the monoclinic materials have at least two/three removable lithium ions that occupy different sites, leading to the non-equivalent site energy and step-type discharge plateaus [48,49].

The present specific capacities is the highest values ever reported among the known $(BO_3)^{3-}$ unit based poly-anion compounds $LiM(BO_3)$, M=Fe, Mn, Co) and their isomorphs till date. Figure 4.5(b) shows typical charge/discharge curves of $Li_3V_2(BO_3)_3$/C at different C-rates in the voltage range between 0.9−4.5 V (vs

Li/Li+) after initial cycle. The charge/discharge curves show the single continuous charge/discharge plateau after initial cycle with remarkably enhancement of charge capacities (From 81.3 mAh g^{-1} to 265.8 mAh g^{-1}) due to the insertion of lithium ions into the crystal lattice of LVB/C to establish the well-ordered LVB/C.

The charge/discharge capacities at 0.05, 0.1, 0.2, 0.5, 1.0, and 2.0 C were found to be 265.8/213.4, 235.1/184.6, 202.1/155.5, 173.8/129.9, 124.6/94.9 and 85.9/55.2, respectively. At the low C-rates (0.05C-0.1C) the discharge capacities were change slightly and the above 0.5 C, the discharge capacity decreases rapidly with increase C-rates because the polarization start to be more prominently at higher C-rates.

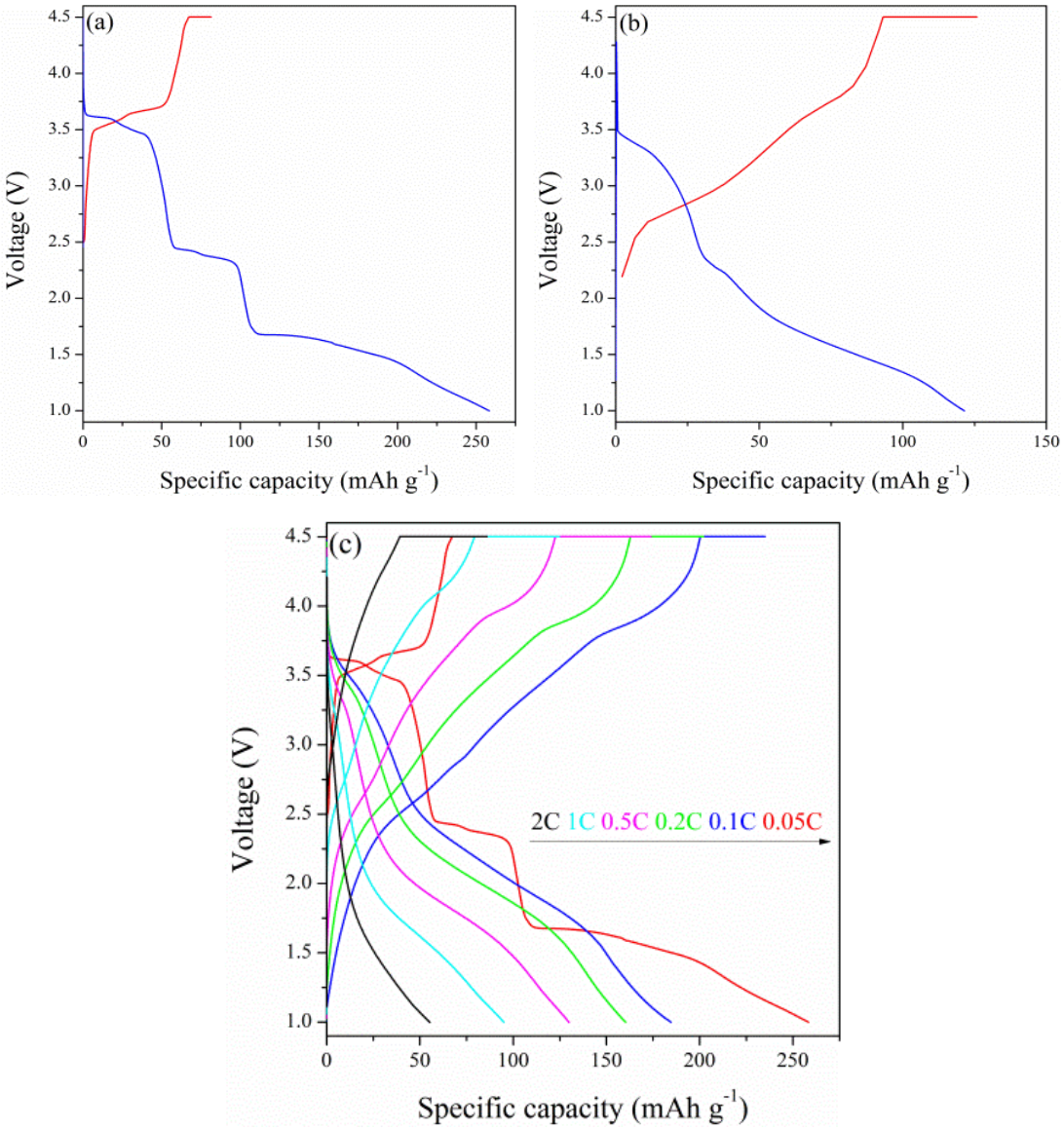

Figure 4.5 (a) 1st charge and discharge curves, (b) 2nd charge and discharge curves of (c) Initial charge and discharge curves of $Li_3V_2(BO_3)_3$/C at various C-rate.

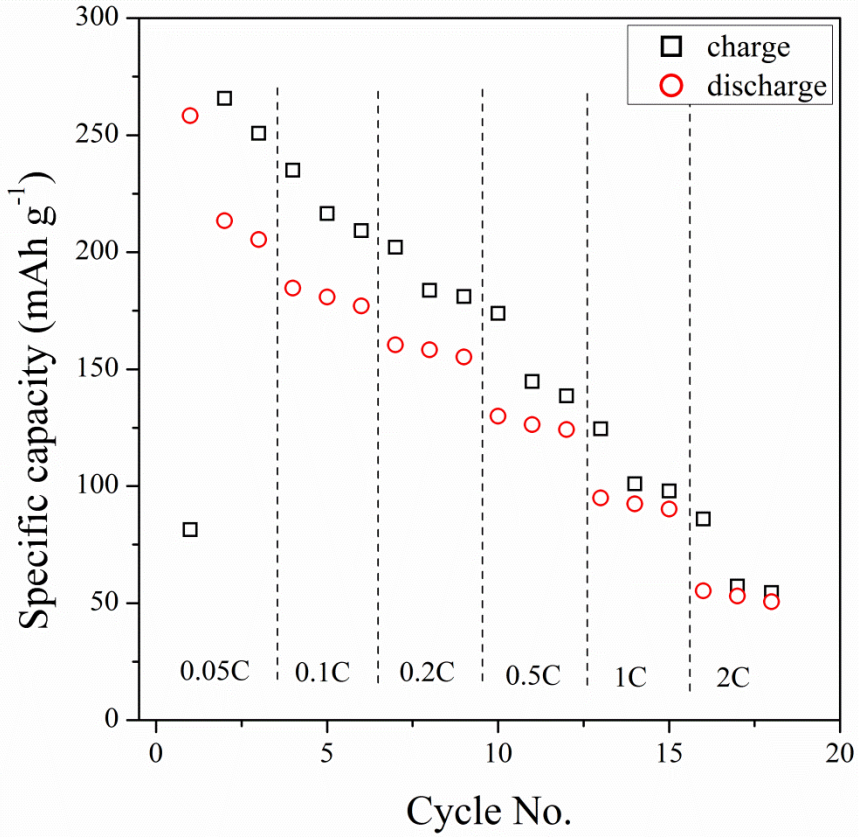

Figure 4.6 Rate performance of $Li_3V_2(BO_3)_3$/C at various C-rate.

The cycling performance of the $Li_3V_2(BO_3)_3$/C at 1 C rate for the 1^{st}, 2^{nd}, 5^{th}, 10^{th} , 15^{th} and 20^{th} is shown in figure 4.7. It is noted that the charge capacity for the 1^{st} cycle is smaller than that of the discharge capacity which showed the similar behavior as reported for the borates cathode materials [50]. After the 1^{st} cycle the successive cycles (2^{nd}, 5^{th}, 10^{th}, 15^{th} and 20^{th}) show the charge/discharge capacity in reversible manner. In the 1^{st}, 2^{nd}, 5^{th}, 10^{th}, 15^{th} and 20^{th} the discharge capacities are 122.1, 121.4, 99.6, 90.7, 84.2 and 79.4 mAh g^{-1} respectively. It is clearly seen that the discharge capacity is continuously decrease. After the 20^{th} cycles, the discharge capacity was remained at 79.4 mAh g-1, which is 65% of the discharge capacity of 1^{st}. Besides from this the stable potential plateau of charge/discharge profiles after 20^{th} cycles indicates the excellent and stable cycling behavior of $Li_3V_2(BO_3)_3$/C.

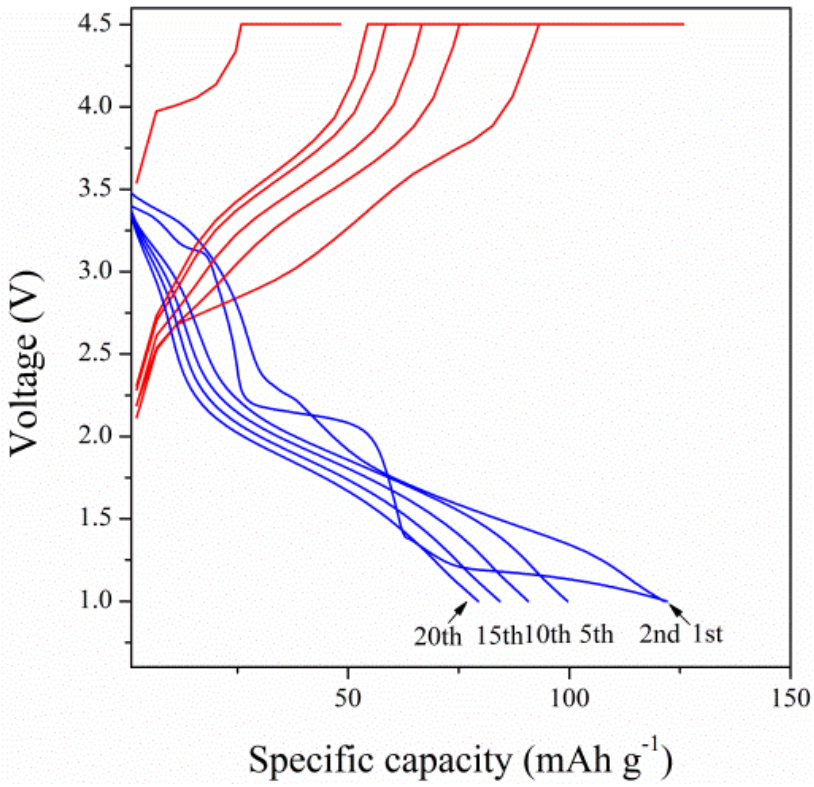

Figure 4.7 Cycle performance of $Li_3V_2(BO_3)_3$/C at 1C.

4.2.2 Cyclic Voltammetry (CV) properties

The Cyclic voltammetry (CV) results were obtained to gain understanding the electrochemical behavior about the charge/discharge profiles of $Li_3V_2(BO_3)_3$/C at the scan rate of 0.05 mV s^{-1}. The five times repeated CV scan results are presented in figure 4.8. The unusual voltage change is observed between the 1st and 2-5th cycles, there is only one oxidation peak and three reduction peaks are appears for the first cycle while the two well defined peaks for both oxidation and reduction peaks are clearly seen for the 2-5th cycles.

The unusual electrochemical behavior of the initial cycle is confirmed via CV scan results with one oxidation peak at the potential 3.74 V and three reduction peaks at the potentials: 3.55, 2.29, and 1.30 V which are good agreement with the positions of the charge/discharge voltage plateaus as observed in figure 4.8(a). There are two oxidation peaks at 2.6 V and 3.3 V with extra oxidation peak at 2.88 V which may be arise due to the impurity phases of $LiVO_3$ and $Li_2B_4O_7$ while the two reduction peaks occur at 1.84 V and 3.43 V respectively. As can be seen, in the 2-5thcycles two pairs of oxidation and reduction peaks appear which are well agreed with the intercalation/de-intercalation of Li^+ via the formation of well-ordered LiV_2O_5 after first irreversible cycle. Moreover, there are no pronounced changes occurs in the shape and peak intensity for the subsequent cycles, indicating that the $Li_3V_2(BO_3)_3$/C has excellent cycling stability and reversibility.

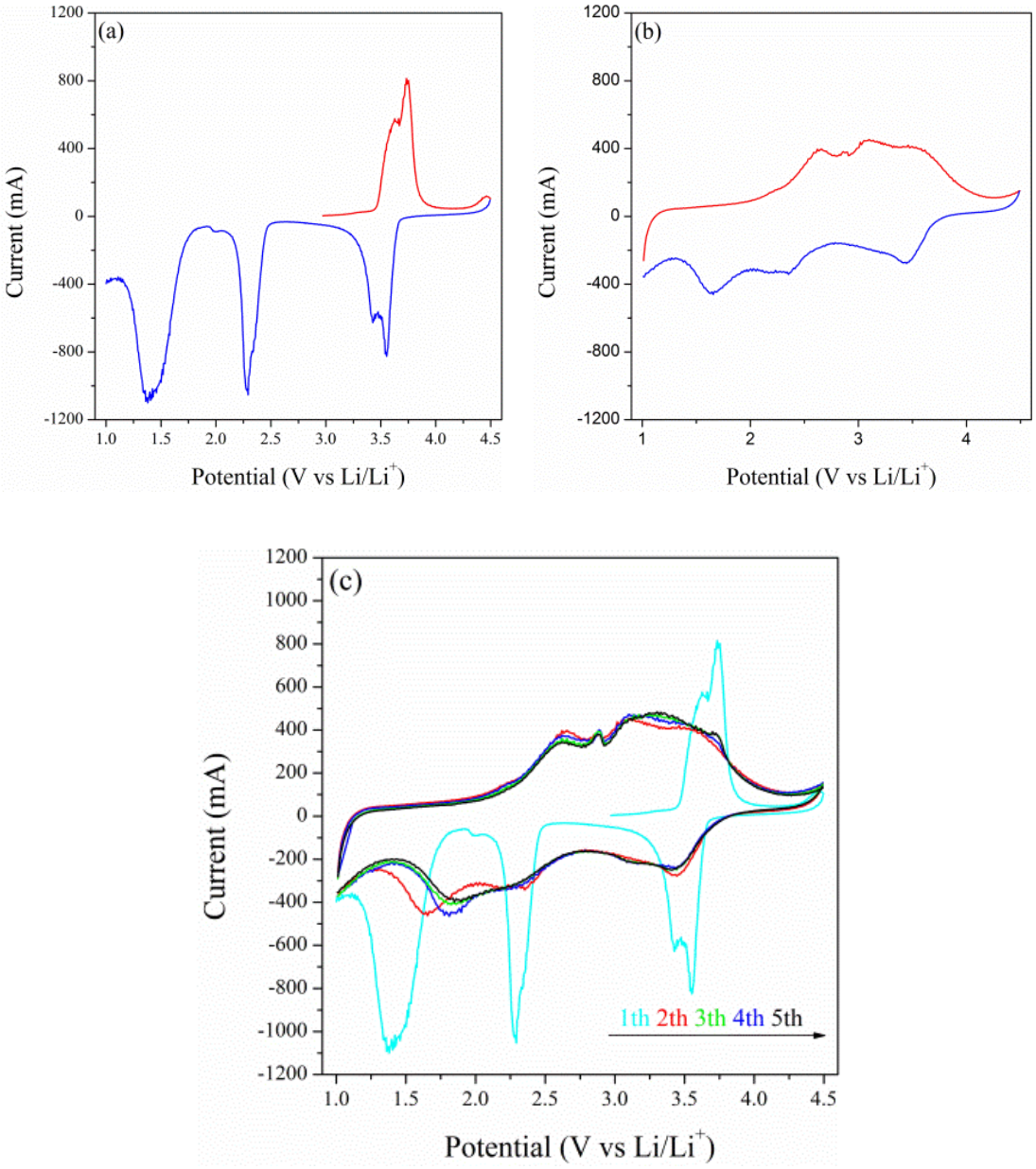

Figure 4.8 Cyclic voltammetry during (d) 1st charge –discharge, (d) 2nd charge-discharge and (c) 1st -5st charge - discharge of $Li_3V_2(BO_3)_3$/C.

4.3 MAS NMR for structural characterization

4.3.1 ^{7}Li, ^{51}V MAS NMR

The information regarding the Li and V in the structural framework of $Li_3V_2(BO_3)_3$/C obtained by the solid-state nuclear magnetic resonance (NMR) spectroscopy. The ^{7}Li and ^{51}V MAS NMR spectra are displayed in figure 4.9. The ^{7}Li MAS NMR shows the existence of a single resonance peak around 3.9 ppm pointed out by arrow and spinning side bands are recognized by asterisks(*) corresponding to the lithium site in $Li_3V_2(BO_3)_3$/C. The presence of single resonance peak of ^{7}Li MAS NMR reveals the single Li site in the structural framework and compares its position to those reported for $Li_3V_2(PO_4)_3$ where they found the three Li environments with three isotropic signals located at 17, 52, and 103 ppm, confirmed the three crystallographic types of lithium ions [51]. The ^{51}V MAS NMR spectrum displayed in the figure 4.9(b) exhibits a broad isotropic resonance at approximately -541.3 ppm with a series of sidebands that span over more than 1500 ppm corresponds to the vanadium site which is consistent with $Li_2V_3O_8$ [52,53]. Both the ^{7}Li and ^{51}V MAS NMR spectra show single lithium and vanadium local environments in $Li_3V_2(BO_3)_3$/C structural framework.

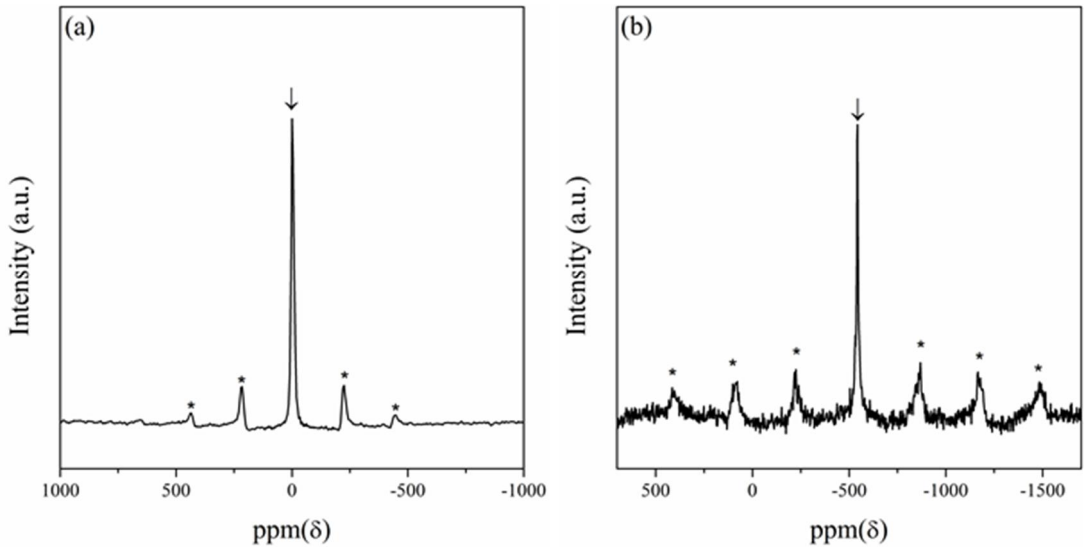

Figure 4.9 (a) ^{7}Li and (b) ^{51}V MAS NMR spectrum of $Li_3V_2(BO_3)_3/C$ at 25kHz. Isotropic peak is marked as arrow and the spinning sidebands are marked with asterisks (*).

5. Conclusions

Combustion method was used to synthesize $Li_3V_2(BO_3)_3$/C cathode material and the improvement of the cathode material properties by elemental analysis and electrochemical measurements was carried out. When $Li_3V_2(BO_3)_3$/C cathode material was synthesized with different sintering temperatures of 450℃, 500℃, 550℃ and 600℃, XRD was confirmed to show the simplest phase at 450℃ and also, XRD analyses shows mixed phase of sintered $Li_3V_2(BO_3)_3$/C at 450℃. SEM and TEM images were used to confirm the porous morphology. The presence and oxidation state of each element was determined through XPS. Solid-state NMR was measured by ^{7}Li and ^{51}V MAS NMR spectroscopy. The single isotropic peak and spinning sideband were confirmed by MAS method. This is probably due to the fact that the material is strongly diamagnetic and has not been affected. As a result, $Li_3V_2(BO_3)_3$/C was synthesized to complete the new material with excellent performance. We confirmed that the material was reversible through rate performance and cyclic voltammetry (CV) tests. This material exhibited excellent performance at low C-rate, but poor performance at high C-rate because the discharge capacity decreases rapidly with increase C-rates because the polarization starts to be more prominently at higher C-rates. Therefore, more research on this is needed.

6. Reference

[1] S. Yin, H. Grondey, P. Strobel, M. Anne, L.F. Nazar, J.Am.Chem.Soc. 125 (2003) 10402-10411.

[2] http://mutuslab.cs.uwindsor.ca/schurko/ssnmr/ssnmr_schurko.pdf.

[3] S. Matsuoka, Chemical Communications. 38 (2009) 5664-5675.

[4] https://nationalmaglab.org/about/around-the-lab/meet-the-probes/mas-probe.

[5] J.D. Biglands, A. Radjenovic, J.P. Ridgway, J.Cardiovasc.Magn.Reson. 14 (2012) 66.

[6] http://medradresource.blogspot.kr/2012/11/what-is-spin-echo-used-for-in-nmr.html.

[7] C.P. Grey, N. Dupré, Chem.Rev. 104 (2004) 4493-4512.

[8] D. Carlier, I. Saadoune, M. Ménétrier, C. Delmas, J.Electrochem.Soc. 149 (2002) A1310-A1320.

[9] L. Davis, I. Heinmaa, B. Ellis, L. Nazar, G. Goward, Physical Chemistry Chemical Physics. 13 (2011) 5171-5177.

[10] Y. Wang, G. Cao, Adv Mater. 20 (2008) 2251-2269.

[12] J.W. Fergus, J.Power Sources. 195 (2010) 939-954.

[13] R. Koksbang, J. Barker, H. Shi, M. Saidi, Solid State Ionics. 84 (1996) 1-21.

[14] J.B. Goodenough, Y. Kim, Chemistry of materials. 22 (2009) 587-603.

[15] http://priusblack.blogspot.kr/2016/09/lithium-ion-fires-explosions-are.html,.

[16] M.D. Bhatt, C. O'Dwyer, Physical Chemistry Chemical Physics. 17 (2015) 4799-4844.

[17] M.M. Thackeray, C. Wolverton, E.D. Isaacs, Energy & Environmental Science 5 (2012) 7854-7863.

[18] M. Armand, J. Tarascon, Nature. 451 (2008) 652-657.

[19] M.J. Armstrong, C. O'Dwyer, W.J. Macklin, J.D. Holmes, Nano Research 7 (2014) 1-62

[20] G. Amatucci, J. Tarascon, L. Klein, Solid State Ionics. 83 (1996) 167-173.

[21] G. Amatucci, J. Tarascon, L. Klein, J.Electrochem.Soc. 143 (1996) 1114-1123.

[22] B. Deng, H. Nakamura, M. Yoshio, J.Power Sources. 180 (2008) 864-868.

[23] S. Lee, S.S. Park, The Journal of Physical Chemistry C. 116 (2012) 25190-25197.

[24] J. Gaubicher, C. Wurm, G. Goward, C. Masquelier, L. Nazar, Chemistry of materials. 12 (2000) 3240-3242.

[25] C. Deng, S. Zhang, S. Yang, Y. Gao, B. Wu, L. Ma, B. Fu, Q. Wu, F. Liu, The Journal of Physical Chemistry C. 115 (2011) 15048-15056.

[26] Z. Gong, Y. Yang, Energy & Environmental Science 4 (2011) 3223-3242.

[27] G. Hautier, A. Jain, H. Chen, C. Moore, S.P. Ong, G. Ceder, Journal of Materials Chemistry. 21 (2011) 17147-17153.

[28] A. Yamada, N. Iwane, Y. Harada, S. Nishimura, Y. Koyama, I. Tanaka, Adv Mater. 22 (2010) 3583-3587.

[29] S. Afyon, D. Kundu, A.J. Darbandi, H. Hahn, F. Krumeich, R. Nesper, Journal of Materials Chemistry A. 2 (2014) 18946-18951.

[30] C.M. Julien, A. Mauger, K. Zaghib, H. Groult, Inorganics. 2 (2014) 132-154.

[31] https://www.bruker.com/fileadmin/user_upload/8-PDF-Docs/MagneticResonance/NMR/brochures/what-is-nmr_brochure_0115_T153283.pdf.

[32] https://en.wikipedia.org/wiki/Nuclear_magnetic_resonance.

[33] http://bionmr.unl.edu/course.php?id=chem991a_-_intro_to_nmr.

[34] D.A. Skoog, F.J. Holler, S.R. Crouch, Principles of instrumental analysis, Cengage learning, 2017.

[35] J.C. Edwards, Process NMR Associates LLC, 87A Sand Pit Rd, Danbury CT. 6810 (2009).

[36] https://en.wikipedia.org/wiki/Solid-state_nuclear_magnetic_resonance Dipolar_coupling.

[37] F. Taulelle, Fundamental principles of NMR crystallography, Wiley Online Library, 2009.

[38] M.H. Levitt, R. Freeman, Journal of Magnetic Resonance (1969). 33 (1979) 473-476.

[39] W. Wang, H. Wang, S. Liu, J. Huang, Journal of Solid State Electrochemistry. 16 (2012) 2555-2561.

[40] Z. Huang, L. Cao, L. Chen, Y. Kuang, H. Zhou, C. Fu, Z. Chen, The Journal of Physical Chemistry C. 120 (2016) 3242-3249.

[41] G. Ali, A. Mehmood, H.Y. Ha, J. Kim, K.Y. Chung, Scientific reports. 7 (2017) 40910.

[42] R. Dedryvere, M. Maccario, L. Croguennec, F. Le Cras, C. Delmas, D. Gonbeau, Chemistry of Materials. 20 (2008) 7164-7170.

[43] H. Yang, X. Wu, M. Cao, Y. Guo, The Journal of Physical Chemistry C. 113 (2009) 3345-3351.

[44] W. Moddeman, A. Burke, W. Bowling, D. Foose, Surf.Interface Anal. 14 (1989) 224-232.

[45] B. Zhang, C. Shen, J. Zheng, Y. Han, J. Zhang, L. Ming, J. Wang, S. Qin, H. Li, J.Electrochem.Soc. 161 (2014) A748-A752

[46] Q. Chen, J. Wang, Z. Tang, W. He, H. Shao, J. Zhang, Electrochim.Acta. 52 (2007) 5251-5257.

[47] Y. Rho, L.F. Nazar, L. Perry, D. Ryan, J.Electrochem.Soc. 154 (2007) A283-A289.

[48] C. Liu, R. Massé, X. Nan, G. Cao, Energy Storage Materials. 4 (2016) 15-58.

[49] S. Yin, H. Grondey, P. Strobel, H. Huang, L.F. Nazar, J.Am.Chem.Soc. 125 (2003) 326-327.

[50] J.C. Kim, D. Seo, G. Ceder, Energy & Environmental Science. 8 (2015) 1790-1798.

[51] A. Castets, D. Carlier, K. Trad, C. Delmas, M. Ménétrier, The Journal of Physical Chemistry C. 114 (2010) 19141-19150.

[52] C.P. Grey, N. Dupré, Chem.Rev. 104 (2004) 4493-4512.

[53] N. Dupré, J. Gaubicher, D. Guyomard, C.P. Grey, Chemistry of materials. 16 (2004) 2725-2733.